Publisher: NPG; Journal: Nature: Nature; Article Type: Biology article
MS nr: 2019-08-12893D

Closed mitosis requires local disassembly of the nuclear envelope

Gautam Dey[1†], Siân Culley[1], Scott Curran[2], Uwe Schmidt[3,4], Ricardo Henriques[1], Wanda Kukulski[5] & Buzz Baum[1,6†]

[1]MRC Laboratory for Molecular Cell Biology, London, UK.

[2]The Francis Crick Institute, London, UK.

[3]Max Planck Institute of Molecular Cell Biology and Genetics, Dresden, Germany.

[4]Center for Systems Biology Dresden, Dresden, Germany.

[5]MRC Laboratory of Molecular Biology, Cambridge, UK.

[6]Institute for the Physics of Living Systems, University College London, London, UK

†e-mail: g.dey@ucl.ac.uk, b.baum@ucl.ac.uk

At the end of mitosis, eukaryotic cells must segregate the two copies of their replicated genome into two new nuclear compartments[1]. They do this either by first dismantling and later reassembling the nuclear envelope in an 'open mitosis' or by reshaping an intact nucleus and then dividing it into two in a 'closed mitosis'[2,3]. Mitosis has been studied in a wide variety of eukaryotes for more than a century[4], but how the double membrane of the nuclear envelope is split into two at the end of a closed mitosis without compromising the impermeability of the nuclear compartment remains unknown[5]. Here, using the fission yeast *Schizosaccharomyces pombe* (a classical model for closed mitosis[5]), genetics, live-cell imaging and electron tomography, we show that nuclear fission is achieved via local disassembly of nuclear pores within the narrow bridge that links segregating daughter nuclei. In doing so, we identify the protein Les1, which is localized to the inner nuclear envelope and restricts the process of local nuclear envelope breakdown to the bridge midzone to prevent the leakage of material from daughter nuclei. The mechanism of local nuclear envelope breakdown in a closed mitosis therefore closely mirrors nuclear envelope breakdown in open mitosis[3], revealing an unexpectedly high conservation of nuclear remodelling mechanisms across diverse eukaryotes.

A key event in the process of cell division in eukaryotes is the partitioning of the nuclear genome into two nuclear compartments. To achieve this, replicated sister chromosomes detach from the

inner nuclear envelope[3], enabling them to be separated from one another through the work of a microtubule-based spindle[6], before being sorted into two new, physically separate nuclei at mitotic exit[Author: Please note that we avoid two-letter abbreviations in the main text, so NE has been expanded throughout.]. Eukaryotic cells have adopted a wide variety of strategies to coordinate nuclear remodelling with chromosome segregation[2]. At one extreme, in open mitosis, cells first disassemble the nuclear lamina and the continuous nuclear envelope at mitotic entry, and then reverse this process by reassembling the structure around separated chromosomes at mitotic exit. At the other extreme, in a closed mitosis, because the nuclear/cytoplasmic compartment barrier remains intact throughout the division process, spindle poles must be inserted into the nuclear envelope[7] to form an intranuclear spindle that can drive chromosome segregation. This spindle is then disassembled as the nuclear envelope is divided into two[8]. These different modes of nuclear division share key features, and despite there being a range of intermediate states[9,10], the resolution of a closed mitosis presents a unique topological challenge. How organisms undergoing closed mitosis divide the double nuclear envelope without compromising nuclear integrity is not currently understood.

To shed light on this process, we chose to study nuclear division in the fission yeast *S. pombe*, which serves as an experimentally tractable example of an organism that undergoes closed mitosis. Previous studies have shown that the *S. pombe* nucleus does not tear at mitotic exit[11], as it does in the related yeast *Schizosaccharomyces japonicus.* Instead, the nucleus constricts to form a dumb-bell shape with a thin nuclear bridge around the anaphase spindle[5]. Whereas the organization and dynamics of the anaphase spindle have been studied in some detail[12–14], it is not known how the nuclear envelope is then remodelled to generate two new nuclei at the end of this process without compromising the compartmental barrier between the nucleus and cytoplasm.

To investigate this question, we used a synthetic nuclear-localized green fluorescent protein (GFP) construct to characterize the dynamics of nuclear fission and to determine the extent to which the nuclear permeability barrier is maintained throughout the process (Fig. 1a, b). Although nuclear GFP levels remained constant throughout the division process (as expected for a closed mitosis), using an automated analysis pipeline described in Extended Data Fig. 2a and Methods, we observed a gradual loss of GFP from the nuclear bridge before nuclear division (Fig. 1b). Notably, this occurred without the visible leakage of GFP from daughter nuclei (Fig.

1a). Imaging nuclear envelope remodelling over the same time period is complicated by the fact that in fission yeast, as in other eukaryotes, the outer face of the nuclear envelope is continuous with the 3D mesh of tubules and sheets constituting the endoplasmic reticulum[15] (Fig. 1c, Extended Data Fig. 1a). To better image this process live, we searched for an effective marker of the inner nuclear envelope. Our search identified the candidate protein SPAC23C4.05c, owing to its homology to the stress-responsive nuclear envelope protein Ish1 (Extended Data Fig. 1c–e) and its strong negative genetic interactions with ESCRTIII proteins[16] (Extended Data Fig. 1b). SPAC23C4.05c localizes exclusively to the nucleoplasmic surface of the inner nuclear envelope throughout the cell cycle (Fig. 1c, Extended Data Fig. 2d, e) without labelling endoplasmic reticulum tubules or cortex. SPAC23C4.05c was also seen concentrated at the stalk of each daughter nucleus during anaphase—a phenotype for which we named the protein Lem-like enriched in stalks (Les1)[Author: Please note that we do not use underlines or upper case for emphasis when defining acronyms.] (see Methods for further details).

Using Les1 as a marker, we were able to follow in detail the dynamic changes in nuclear shape that accompany spindle elongation, as the single nucleus divides into two via a characteristic dumb-bell-shaped intermediate (Fig. 1d). The kinetics of spindle elongation are highly reproducible[17], allowing us to align single-cell trajectories to the time point at which the spindle reaches its maximum length (see Methods). At early stages of bridge formation, Les1 concentrated in stalks originating at the neck of each daughter nucleus (Fig. 1d, e). At maximum spindle elongation, Les1 was visibly depleted from the midzone of the bridge (Fig. 1d), a process that was followed, within a few seconds, by the breakage of the spindle (Fig. 1d, Extended Data Fig. 2b).

These observations pointed to the midzone of the bridge as the site where nuclear fission probably occurs. We then used correlative light microscopy and electron tomography of cells labelled with both Les1–mNeonGreen and mCherry–Atb2 (Fig. 2a) to characterize early and late nuclear bridges (Fig. 2b, c, Extended Data Fig. 3a). In early bridges, the nuclear envelope was observed surrounding the spindle (narrowing at the base of the stalks and widening towards the midzone) and was studded with nuclear pores (Fig. 2b). At an intermediate stage, the nuclear pores were completely excluded from the stalk and clustered in a central bulge (Extended Data Fig. 3b). By contrast, in late stage bridges, while the nuclear envelope still enveloped the spindle within stalks, there was no evidence of a continuous nuclear envelope in the midzone region of

the bridge. Instead, spindle microtubules were seen projecting out of the two newly formed daughter nuclei into the cytoplasm, through stalk membranes that lacked nuclear pores (Fig. 2c). All that appeared to be left of the central part of the nuclear bridge at this stage were fragments of membrane, an observation that explains the loss of nuclear GFP from the midzone of the late anaphase bridge (Fig. 1).

If the nuclear envelope in the central region of the bridge is disassembled to induce nuclear division as suggested by this unexpected observation, how is this distinct midzone region specified? A clue came from two observations made using electron tomography. First, nuclear pores within early-stage bridges were found to be physically too close to spindle microtubules to possess a full nuclear basket, on the basis of steric considerations (Extended Data Figs. 2d, e, 3c). Second, nuclear pores were completely absent from stalks in late-stage bridges (Fig. 2c). Building on these observations, when we tracked various components of the nuclear pore complex (NPC)—a complex of individual proteins referred to as nucleoporins or 'Nups' Extended Data Fig. 2d—through nuclear division by light microscopy, we discovered that the pores that enter the bridge are completely devoid of the nuclear basket components Alm1 and Nup211 (Fig. 3a, Extended Data Fig. 4a–c). NPCs were also visibly depleted from stalk regions of the bridge where Les1 is concentrated (Fig. 3b, c, Extended Data Fig. 5a). Instead, as previously reported[18,19], NPCs were found concentrated in the central bulging section of the bridge, where Les1 levels are low (Fig. 3b, c). Even here, the movement of NPC clusters within the midzone appeared constrained by the stalks on either side (Fig. 3c).

Several lines of evidence indicate that Les1 accumulation, and the concomitant corralling of NPCs, requires a close association of the nuclear envelope with spindle microtubules but is not contingent on the formation of a normal bridge midzone. First, occasional 'stray' NPC clusters located distal to the midzone always correspond to areas of local Les1 depletion and local bridge dilation (Extended Data Fig. 5c–f). Second, in cells with excess nuclear envelope that generate thicker, floppy bridges, Les1 cannot form stalks and NPCs are no longer restricted to the midzone (Extended Data Fig. 6a). Finally, aberrant tubular projections containing spindle microtubules induced either by reducing nuclear envelope surface area or by acutely inhibiting Aurora kinase activity before cells enter mitosis (see Methods), accumulate Les1 and lack NPCs (Extended Data Fig. 6b, c). Together, these results indicate that the stalks, defined by Les1

accumulation at sites of microtubule–membrane contact within the bridge, function to restrict a population of basketless NPCs to the bridge midzone.

In an open mitosis, the stepwise removal of NPCs leads to nuclear envelope fenestration and loss of structural integrity during nuclear envelope breakdown[10] (NEB). We observed precisely this sequence of events in the *S. pombe* bridge midzone, in a process that we term 'local NEB'. Thus, in the few minutes following dumb-bell collapse, as the nuclear-localization signal (NLS)–GFP intensity in the nucleus was seen disappearing from the bridge (Fig. 3e), NPCs were gradually lost from the midzone. This process began with the loss of nuclear ring Nups (Nup60) and was completed with the loss of transmembrane Nups (Cut11) (Fig. 3d, e, Extended Data Fig. 5g–i). Fast imaging revealed distinct clusters of NPCs disappearing at different times; this order of events was preserved within any single bridge (Extended Data Fig. 5i). Of note, whereas this was independent of Les1 itself (Extended Data Fig. 7d, e), both NPC disassembly and local NEB could be completely arrested by deletion of the importin Imp1[19] (Fig. 3f, g, Extended Data Fig. 6d). Since local NEB precedes spindle disassembly (Fig. 2c, 3d, e), this also enables us to reinterpret the previously described Imp1-mutant spindle phenotype[19]. Our results show that Imp1-dependent removal of bridge NPCs and local nuclear envelope breakdown expose spindle microtubules to the cytoplasm, where cytoplasmic factors trigger their timely disassembly.

What is the function of Les1 in this context? In support of the idea that the site of NEB is restricted to the bridge midzone by Les1-defined stalks, the spatial organization of NPCs in the bridge was completely lost in the *les1Δ* strain. Light (Fig. 4a, Extended Data Fig. 7f) and electron tomography (Fig. 4c, Extended Data Fig. 7a, b) of these cells showed that NPC components were uniformly distributed in both early- and late-stage bridges, leading to the onset of local NEB at a random location along the bridge (Extended Data Fig. 7f). Daughter nuclei in the *les1Δ* strain also suffered transient leakages at the time of maximum spindle elongation, as measured by loss of nuclear NLS–GFP (Fig. 4a, b); this typically occurred in only one of the two daughter-cell nuclei (Fig. 4a, b). These leaks were rapidly repaired in a manner that does not depend on Les1 (Fig. 4a) – an observation that explains the lack of a growth defect in the *les1Δ* strain. Instead, the repair process was associated with recruitment of the ESCRTIII protein Cmp7 (Fig. 4d) to sites of local NEB[20] (Fig. 4d, Extended Data Fig. 8b, c). In line with this, *les1Δ* is synthetically near-lethal when combined with deletions in *cmp7* or *lem2* (Extended Data Fig. 8d,

e), encoding the gene for Lem2, the binding partner of Cmp7. These observations are also consistent with the highly conserved role for ESCRTIII proteins in nuclear envelope sealing[21–24] and repair[25,26] across metazoan and fungal mitoses.

Together, these data suggest that Les1 stalks functionally isolate daughter nuclei from the process of Imp1-dependent local NEB at the centre of the bridge (Extended Data Fig. 8g). Consistent with this hypothesized role for Les1, deleting Les1 does not strongly affect the kinetics of NPC disassembly (Extended Data Fig. 7d, e) or average inter-NPC spacing (Extended Data Fig. 7b). Instead, Les1 probably acts to create a seal by gathering the inner nuclear envelope tightly around the spindle, leading to the segregation of excess membrane and bulky NPCs into the characteristic bulge at the centre of the bridge in wild-type cells, a structure that is conspicuously absent from *les1Δ* tomograms (Fig. 4c). Consistent with this model, treating *les1Δ* cells with cerulenin to increase membrane tension in the bridge (by inhibiting fatty acid biosynthesis in the endoplasmic reticulum[27]) forces NPCs back to the centre to rescue the nuclear-leakage phenotype in the proportion of cells that are able to form a bridge (Fig. 4e, Extended Data Fig. 8f). Therefore, Les1 performs a critical role in nuclear division in *S. pombe* by ensuring that, while nuclei are topologically open to the cytoplasm at this stage of mitosis, the compartment boundary itself remains effectively closed (Fig. 4f, g).

In summary, we have identified Les1, a protein that positions the site of nuclear fission during nuclear division in *S. pombe*. Through the study of Les1 localization and its deletion mutant, we describe a process of local nuclear envelope breakdown that reveals an unexpectedly close similarity between the remodelling of the nuclear envelope in open and closed mitosis (Fig. 4g). In both cases, the new nuclear compartment is remodelled as the result of NPC disassembly. Thus, the key difference between mitotic strategies across the eukaryotic tree[28] may simply be one of degree, depending on the timing and localization of NPC disassembly.

Online content

Any methods, additional references, Nature Research reporting summaries, source data, extended data, supplementary information, acknowledgements, peer review information; details of author contributions and competing interests; and statements of data and code availability are available at [Article DOI].

Received 10 September 2019; accepted 21 May 2020

<jrn>1. LaJoie, D. & Ullman, K. S. Coordinated events of nuclear assembly. *Curr. Opin. Cell Biol.* **46**, 39–45 (2017). Medline CrossRef</jrn>

<jrn>2. Sazer, S., Lynch, M. & Needleman, D. Deciphering the evolutionary history of open and closed mitosis. *Curr. Biol.* **24**, R1099–R1103 (2014). Medline CrossRef</jrn>

<jrn>3. Ungricht, R. & Kutay, U. Mechanisms and functions of nuclear envelope remodelling. *Nat. Rev. Mol. Cell Biol.* **18**, 229–245 (2017). Medline CrossRef</jrn>

<jrn>4. Yanagida, M. The role of model organisms in the history of mitosis research. *Cold Spring Harb. Perspect. Biol.* **6**, a015768 (2014). Medline CrossRef</jrn>

<jrn>5. Zhang, D. & Oliferenko, S. Remodeling the nuclear membrane during closed mitosis. *Curr. Opin. Cell Biol.* **25**, 142–148 (2013). Medline CrossRef</jrn>

<jrn>6. Walczak, C. E., Cai, S. & Khodjakov, A. Mechanisms of chromosome behaviour during mitosis. *Nat. Rev. Mol. Cell Biol.* **11**, 91–102 (2010). Medline CrossRef</jrn>

<jrn>7. Tamm, T. et al. Brr6 drives the *Schizosaccharomyces pombe* spindle pole body nuclear envelope insertion/extrusion cycle. *J. Cell Biol.* **195**, 467–484 (2011). Medline CrossRef</jrn>

<jrn>8. Boettcher, B. & Barral, Y. The cell biology of open and closed mitosis. *Nucleus* **4**, 160–165 (2013). Medline CrossRef</jrn>

<jrn>9. Harel, A. et al. Persistence of major nuclear envelope antigens in an envelope-like structure during mitosis in *Drosophila melanogaster* embryos. *J. Cell Sci.* **94**, 463–470 (1989). Medline</jrn>

<jrn>10. Lénárt, P. et al. Nuclear envelope breakdown in starfish oocytes proceeds by partial NPC disassembly followed by a rapidly spreading fenestration of nuclear membranes. *J. Cell Biol.* **160**, 1055–1068 (2003). Medline CrossRef</jrn>

<jrn>11. Gu, Y., Yam, C. & Oliferenko, S. Divergence of mitotic strategies in fission yeasts. *Nucleus* **3**, 220–225 (2012). Medline CrossRef</jrn>

<jrn>12. Ding, R., McDonald, K. L. & McIntosh, J. R. Three-dimensional reconstruction and analysis of mitotic spindles from the yeast, *Schizosaccharomyces pombe*. *J. Cell Biol.* **120**, 141–151 (1993). Medline CrossRef</jrn>

<jrn>13. Ward, J. J., Roque, H., Antony, C. & Nédélec, F. Mechanical design principles of a mitotic spindle. *eLife* **3**, e03398 (2014). Medline CrossRef</jrn>

<jrn>14. Loiodice, I. et al. Quantifying tubulin concentration and microtubule number throughout the fission yeast cell cycle. *Biomolecules* **9**, 86 (2019). Medline CrossRef</jrn>

<jrn>15. Zhang, D., Vjestica, A. & Oliferenko, S. The cortical ER network limits the permissive zone for actomyosin ring assembly. *Curr. Biol.* **20**, 1029–1034 (2010). Medline CrossRef</jrn>

<jrn>16. Frost, A. et al. Functional repurposing revealed by comparing *S. pombe* and *S. cerevisiae* genetic interactions. *Cell* **149**, 1339–1352 (2012). Medline CrossRef</jrn>

<jrn>17. Krüger, L. K., Sanchez, J.-L., Paoletti, A. & Tran, P. T. Kinesin-6 regulates cell-size-dependent spindle elongation velocity to keep mitosis duration constant in fission yeast. *eLife* **8**, e42182 (2019). Medline CrossRef</jrn>

<jrn>18. Flor-Parra, I. et al. Importin α and vNEBD control meiotic spindle disassembly in fission yeast. *Cell Rep.* **23**, 933–941 (2018). Medline CrossRef</jrn>

<jrn>19. Lucena, R. et al. Nucleocytoplasmic transport in the midzone membrane domain controls yeast mitotic spindle disassembly. *J. Cell Biol.* **209**, 387–402 (2015). Medline CrossRef</jrn>

<jrn>20. Gatta, A. T. & Carlton, J. G. The ESCRT-machinery: closing holes and expanding roles. *Curr. Opin. Cell Biol.* **59**, 121–132 (2019). Medline CrossRef</jrn>

<jrn>21. Olmos, Y., Hodgson, L., Mantell, J., Verkade, P. & Carlton, J. G. ESCRT-III controls nuclear envelope reformation. *Nature* **522**, 236–239 (2015). Medline CrossRef</jrn>

<jrn>22. Vietri, M. et al. Spastin and ESCRT-III coordinate mitotic spindle disassembly and nuclear envelope sealing. *Nature* **522**, 231–235 (2015). Medline CrossRef</jrn>

<jrn>23. Pieper, G. H., Sprenger, S., Teis, D. & Oliferenko, S. ESCRT-III/Vps4 controls heterochromatin–nuclear envelope attachments. *Dev. Cell* **53**, 27–41.e6 (2020). CrossRef Medline</jrn>

<jrn>24. von Appen, A. et al. LEM2 phase separation promotes ESCRT-mediated nuclear envelope reformation. *Nature* **582**, 115–118 (2020). CrossRef Medline</jrn>

<jrn>25. Gu, M. et al. LEM2 recruits CHMP7 for ESCRT-mediated nuclear envelope closure in fission yeast and human cells. *Proc. Natl Acad. Sci. USA* **114**, E2166–E2175 (2017). Medline CrossRef</jrn>

<jrn>26. Thaller, D. J. et al. An ESCRT–LEM protein surveillance system is poised to directly monitor the nuclear envelope and nuclear transport system. *eLife* **8**, e45284 (2019). Medline CrossRef</jrn>

<jrn>27. Yam, C., He, Y., Zhang, D., Chiam, K.-H. & Oliferenko, S. Divergent strategies for controlling the nuclear membrane satisfy geometric constraints during nuclear division. *Curr. Biol.* **21**, 1314–1319 (2011). Medline CrossRef</jrn>

<jrn>28. McIntosh, J. R., Roos, U. P., Neighbors, B. & McDonald, K. L. Architecture of the microtubule component of mitotic spindles from *Dictyostelium discoideum*. *J. Cell Sci.* **75**, 93–129 (1985). Medline</jrn>

[Author: Please ensure that the following information is included in the figure legends where relevant. Sample size (exact *n* number); a statement of replicability (how many times was experiment replicated in the lab); description of sample collection (clarify whether technical or biological replicates and include how many animals, litters, cultures, etc.); state the statistical test used and give *P* values; define centre values (median or average) and error bars. For figures/images that are reproduced or adapted from a third party, it is important that you confirm that permission has been obtained and that appropriate acknowledgement of the copyright holder is given.]

Fig. 1 | Les1 domains define the site of nuclear division. a, An *S. pombe* cell (dotted outline) expressing a synthetic NLS–GFP construct undergoing mitosis. Panels are maximum-intensity projections of confocal images acquired every 30 s. Representative of more than 50 cells across 5 biological repeats. Dotted vertical lines represent maximum spindle length (spindle max, $t = 0$). **b**, Mean (darker lines) and standard deviations (lighter bands) of averaged single-cell traces

(from 11 cells at t = 300 to 19 cells at t = 0, from 2 strains) aligned at spindle max (t = 0) and normalized to daughter nuclear intensity at t = 0. **c**, Single-plane Airyscan reconstructions of live cells at various stages of the cell cycle expressing a synthetic endoplasmic reticulum-localized mCherry construct (AHDL) and Les1 tagged with mNeonGreen at the endogenous locus. Green arrowheads mark the boundaries of the Les1 stalks, visible in late anaphase. Representative of more than 10 cells across 2 biological and 8 technical repeats. **d**, Reconstructions using super-resolution radial fluctuations (SRRF) at 28-s intervals on single-plane confocal slices of a cell undergoing anaphase and expressing Atb2–mCherry (tubulin) and Les1–mNeonGreen tagged at the endogenous loci. Green arrowheads mark Les1 stalk boundaries, which first become visible in mid-anaphase. Representative of more than 10 cells across 2 biological and 8 technical repeats. **e**, Les1 intensity in stalks (1.5 μm from the nuclear periphery) over time: mean (darker line) and standard deviations (lighter band) of between 11 (t = 300) and 36 (t = 0) single-cell traces, aligned at spindle max (t = 0) and normalized to maximum bridge intensity. Scale bars, 2 μm.

Fig. 2 | Nuclear division occurs by local nuclear envelope breakdown. a, Representative SRRF reconstructions from single-plane confocal slices of cells in early (left) and late (right) anaphase, expressing Les1–mNeonGreen and Atb2–mCherry (tubulin) tagged at the endogenous loci. Note that intact spindle microtubules persist in the late anaphase bridge despite midzone clearance of Les1. Representative of more than 10 cells across 2 biological and 8 technical repeats. Scale bar, 2 μm. **b**, Virtual slice through electron tomogram (left) and 3D segmentation model (right) of early anaphase bridge. Nuclear envelope, green; microtubules, magenta. The outlined region is magnified on the left. Arrowheads indicate nuclear pores. One technical repeat. Scale bars, 100 nm. **c**, Full and clipped views of 3D segmentation models of late anaphase bridges (nuclear envelope, green; microtubules, magenta), superimposed on virtual slices through electron tomograms, shown without model in second from left. Magnified regions (left) are different virtual slices of the region indicated by white outlines. Magenta arrowheads indicate microtubules, green arrowheads indicate stalk tip and limit of intact nuclear envelope, and blue arrowheads indicate nuclear pores. 2 representatives of 5 technical repeats. Scale bars, 100 nm.

Fig. 3 | Les1-restricted stepwise NPC disassembly drives local NEB. a, *S. pombe* expressing Alm1–mNeonGreen and Cut11–mCherry, maximum-intensity projections of confocal images acquired every 60 s. Scale bar, 2 μm. Representative of more than 30 cells across 3 biological

repeats. **b**, iSIM images of cells expressing Cut11–mCherry and Les1–mNeonGreen. Scale bar, 2 μm. Representative of more than 10 cells across 2 biological and 10 technical repeats. **c**, Kymograph of intensities averaged across a single confocal slice of a dividing cell (white rectangular box in inset) expressing Cut11–mCherry and Les1–mNeonGreen and imaged at three frames per second followed by denoising. Magenta arrows indicate a mobile but corralled NPC cluster. Representative of more than 10 cells across 2 technical repeats. **d**, Maximum intensity projections of confocal images of cells expressing Cut11–GFP and Atb2–mCherry and acquired at 10-s intervals. Scale bars, 2 μm. Representative of more than 30 cells across 3 biological repeats. **e**, Averaged normalized-intensity traces for NLS–GFP (between 22 cells at $t = -300$ and 37 cells at $t = 0$), Nup60–mNeonGreen (between 11 cells at $t = -300$ and 34 cells at $t = 0$) and Cut11–mCherry (between 11 cells at $t = -300$ and 34 at $t = 0$), aligned by spindle max ($t = 0$). The dotted orange line indicates single exponential fit to NLS–GFP average. Data from two strains were combined on the basis of the analysis described in Extended Data Fig. 6b. **f**, Confocal maximum-intensity projections of *imp1*Δ cells expressing Les1–mNeonGreen and Cut11–mCherry in the presence (bottom) or absence (top) of 5 μM latrunculin A (LatA). Magenta arrows indicate persistent midzone Cut11 clusters. Scale bar, 2 μm. Representative of more than 20 cells across 2 biological and 4 technical repeats. **g**, Confocal maximum-intensity projections of *imp1*Δ cells expressing Alm1–mNeonGreen and Cut11–mCherry. Magenta arrows indicate persistent midzone Cut11 clusters. Representative of more than 20 cells across 2 biological repeats. Scale bar, 5 μm.

Fig. 4 | Les1 isolates nuclei from local NEB. a, Maximum-intensity projections of spinning-disk confocal images of cells expressing Nup60–mCherry tagged at the endogenous locus and NLS–GFP, either wild type (top) or carrying a *Les1* deletion (bottom), imaged at 30-s intervals. Orange arrows indicate sites of NLS–GFP leakage from one or both daughter nuclei. Representative of more than 50 cells across 4 biological repeats. Scale bars, 2 μm. **b**, Single-cell intensity traces for wild-type (top) and *les1*Δ cells (bottom), indicating intensity in each daughter nucleus, aligned at spindle max (dotted line, $t = 0$) and normalized individually to maximum intensity. Orange bar and text indicate the number of leaky nuclei. **c**, Virtual slices through electron tomograms of a dividing *les1*Δ cell. The approximate overlap in field of view of the tomograms is indicated by dashed lines. NPCs are indicated by blue arrowheads. Scale bars, 100 nm. Representative of 2 technical repeats. **d**, Confocal maximum-intensity projections of

*les1*Δ cells expressing Cmp7–mNeonGreen and Nup60–mCherry. Representative of more than 20 cells across 3 biological repeats. Scale bar, 2 μm. **e**, *les1*Δ cells expressing NLS–GFP and Nup60–mCherry, in the presence (bottom) or absence (top) of 10 μM cerulenin. Orange arrows indicate sites of NLS–GFP leakage. Representative of more than 40 cells across 3 biological repeats. Scale bar, 5 μm. **f**, Schematic indicating relative intensity levels of key readouts of the nuclear division process, aligned relative to spindle max. **g**, Schematic illustrating the process of local NEB and the role of Les1 in structuring the bridge.

[Author: Please ensure that the following information is provided in the Methods section where relevant. Animal experiments require: statement about randomization; statement about blinding; statement of sex, age, species and strain of animals; statement of IRB approval for live vertebrate experimentation. For experiments involving humans: statement of IRB approval; statement of informed consent; statement of consent to publish any photos included in figures. Randomized clinical trials require trial registration. We recommend that detailed protocols are deposited in Protocol Exchange, or a similar repository. If custom computer code has been used and is central to the conclusions of this paper, please insert a section into the Methods titled 'Code availability' and indicate within this section whether and how the code can be accessed, including any restrictions to access.]

[Author: We assume no power analysis was done to estimate sample size; per our reporting guidelines we will include the statement 'No statistical methods were used to predetermine sample size.' Please edit if appropriate.]

[Author: In order to address the issue of cell line misidentification and cross-contamination, for any cell lines mentioned in the paper please provide source of the cell lines and indicate whether the cell lines have been correctly identified/authenticated (if so, by what methods). Also, please state whether cell lines have been tested for mycoplasma contamination.]

[Author: We assume there was no randomization; per our reporting guidelines, we will include the statement "The experiments were not randomized". Also, we assume that there was no blinding; per our reporting guidelines, we will include the statement "The investigators were not blinded to allocation during experiments and outcome assessment". Please edit either of these statements if necessary.]

METHODS

Phylogenetics and protein bioinformatics

Secondary structure models for Les1 were generated using the homology modelling and threading software tool I-TASSER[29,30] (https://zhanglab.ccmb.med.umich.edu/I-TASSER/). All sequence homology searches were carried out using a local installation of the HMMER suite of profile-HMM search tools[31] (http://hmmer.org/). Uniprot IDs for sequences analysed in Supplementary Fig. 1 are: O94559 (Les1_Sp), S9RL50 (Les1_So), S9VS84 (Les1_Scr), B6JWA6 (Les1_Sj), Q9Y7X6 (Ish1_Sp), S9PR74 (Ish1_So), S9X3G6 (Ish1_Scr), B6K568 (Ish1_Sj) and Q03104 (MSC1_*S.cerevisiae*). MAFFT[32,33] (https://mafft.cbrc.jp/alignment/software/) was used to generate sequence alignment with the following command-line options: mafft–maxiterate 1000–localpair < infile.fasta> > <outfile.align>.

Both trimmed and untrimmed alignments were used to generate phylogenetic trees, though in the case of Les1 this did not significantly affect the resulting trees. Alignments were trimmed, using TrimAl[34] (http://trimal.cgenomics.org/trimal) with these command-line options: trimAl/source/trimal -in < infile.align> -gt 0.6 -cons 40 -phylip -out < outfile.trim>.

Maximum-likelihood trees were inferred using IQTREE[35,36] 1.6 (http://www.iqtree.org/), run using the model test function (for Extended Data Fig. 1d, LG + G4) and 1,000 bootstraps: iqtree-omp-1.5.4-MacOSX/bin/iqtree-omp -nt 4 -s <infile.trim> -m TEST -bb 1000 -redo

Conserved motifs were detected in alignments through comparisons with the PFAM database[37,38] (https://pfam.xfam.org/). Selected regions of alignments were displayed using ESPript3[39] (http://espript.ibcp.fr) and default options. Although Ish1 and Les1 are annotated to be type I LEA domain proteins (Uniprot: https://www.uniprot.org/uniprot/Q9Y7X6), no homology or profile HMM similarity was detected to any LEA domain families. Instead, the easily detected but poorly characterized Ish1 motif (PFAM PF10281), present in two copies in both SPAC23C4.05c and Ish1 (as well as *Saccharomyces cerevisiae* MSC1; Extended Data Fig. 1c–e[Author: Please confirm whether this is in the Extended Data or Supplementary Information.]), bears similarity to the widely conserved HeH/LEM (PFAM PF12949) and SAP (PFAM PF02037) domains. To reflect this finding, we settled on the name Lem-like enriched in

stalks (Les1) for the *S. pombe* protein SPAC23C4.05c and its best-match orthologues in *Schizosaccharomyces* species.

S. pombe culture

S. pombe cells were cultured using standard methods[40,41] on solid (YES agar) and liquid (YES) rich growth media (ForMedium), at a growth temperature of 32 °C unless stated otherwise. All experiments were performed in exponential growth at 32 °C with at least 48 h of growth (>20 generations) in liquid YES before plating for live imaging. For live imaging, uncoated 35-mm dishes with polymer coverslips (no. 1.5 coverslip, 180 μm thick, Ibidi) were first coated with 1 mg ml^{-1} soybean lectin (in water, aliquots stored at −80 °C, Sigma-Aldrich) for 15 min. After washing away the excess lectin with fresh YES, cells drawn from exponentially growing liquid cultures were allowed to settle for 30 min in a minimum volume of 500 μl YES. The entire plating volume was replaced with 1 ml of fresh YES prewarmed to 32 °C before transfer to the microscope. For drug treatment experiments, latrunculin A (Sigma-Aldrich), cerulenin (Sigma-Aldrich) and 1NM-PP1 (Calbiochem) were added to YES at 5 μM (10 mM stock in DMSO), 10 μM (10 mM stock in DMSO) and 5 nM (1 mM stock in DMSO), respectively. The maximal amount of DMSO (1/1,000 in YES) added to cells across conditions had no detectable effect on the kinetics of nuclear division—thus, to ease direct kinetic comparisons across all strains and experiments in the paper, drug-treated cells were compared with untreated controls. For cell culture for electron tomography experiments, see ‘Correlative fluorescence microscopy and electron tomography’.

Plasmids and *S. pombe* strain construction

The full genotypes of all strains used in this study are presented in Extended Data Table 1. Strains generated specifically for this study were constructed using standard methods[40,41] for gene editing and crossing. Gene deletions and tagging were performed as previously described[42] for PCR-based gene targeting, using standard primers designed with the Bahler lab web-interface scripts (http://bahlerlab.info/resources/), pFA6a vector templates carrying hygromycin- or kanamycin-resistance cassettes, and transformation using the lithium acetate method[43]. Antibiotic-resistant clones generated by this method were verified by PCR of the gene locus being targeted as well as fluorescence microscopy, if applicable. The exception to the standard workflow was for the pFA6a-mNeonGreen vectors used in this study, which carry a non-

standard linker upstream of the mNeonGreen coding sequence. Instead of the standard 20-mer (CGGATCCCCGGGTTAATTAA) forward linker, these require a 21-mer forward linker (GATTCTGCTGGATCAGCTGGC). The reverse linker remains unchanged. One new pFA6a vector derivative was generated for this study, replacing the mCherry coding sequence in pFA6a-mCherry:Hph with the coding sequence for the photo-switchable fluorescent protein mEOS3.2[44] (Addgene) by standard restriction-digestion cloning (using restriction enzymes BamHI and AscI; NEB). This vector is available upon request. Crosses were performed by random spore analysis[40,41] followed by marker selection (hygromycin or kanamycin resistance, ura/leu auxotrophy, or sensitivity to 5 μM 1NM-PP1 (Calbiochem) for strains carrying the *Ark1-as3* allele, as appropriate) followed by additional screening for fluorescence, if applicable. The crosses shown in Extended Data Fig. 8d, e were carried out using tetrad dissection[45], with each colony grown from a single spore. In brief, cells were mated on low-nitrogen medium (EMM-nitrogen) to produce tetrads of four haploid spores. After 2 days, cells were streaked onto nutrient-rich medium (YES) for 2–3 h to degrade the protective membrane surrounding each tetrad. Individual spores were isolated using a Singer MSM300 Tetrad Micro dissecting unit. C-terminal truncation constructs with C-terminal mNeonGreen tags (Extended Data Fig. 8a) were generated at endogenous loci using the standard PCR-based method as described above, but with the following left-hand/forward primers: Les1(1–94), 5′-ATTCTTGGCCTCAACGAAAGCTTGATGACTTTCTCCAAAATCATGGGGTAAAGTCACTGGACGTTCCTCCTATCGAGACTGATTCTGCTGGATCAGCTGGC-3′; Les1(1–204), 5′-CCACCAATGATGAGTTGGAATCCTGGTCAAATAATCTACTCCTTTCTATGTTGGATCAGAAAAACATTACAGTACCAATTGATTCTGCTGGATCAGCTGGC-3′; and Les1(1–291) 5′-TTTCTGTTCTTTCACCTCGGGAAACTCTTTTGAAAGAAGCATACGCTAACCGCTTCACACCGCGTGTAATGATTGCCTCCGATTCTGCTGGATCAGCTGGC-3′.

These truncation sites were selected in order to delete either both Ish1 motifs and the C2H2 Zn finger, or the second Ish1 motif and the Zn finger, or just the Zn finger, with care taken to avoid truncating the protein in the middle of predicted secondary structural elements such as alpha-helices. The first two constructs, Les1 (1–94) and Les1 (1–204), did not generate any detectable expression by fluorescence microscopy. The localization pattern of the third construct Les1 (1–291) is shown in Extended Data Fig. 8a.

Live-cell fluorescence microscopy

All strains were imaged live in regular growth medium (YES) in glass-bottom dishes (see *S. pombe* culture) within stage-top incubation chambers held at 32 °C. No single dish was used for experiments lasting longer than 3 h from the time of plating. Four microscopes were used for this study: two spinning-disk confocal systems, a Nikon TiE wide-field system with a VT-iSIM module and a Zeiss LSM880 with an Airyscan module. The first spinning-disk microscope consists of a Nikon TiE inverted stand attached to a Yokogawa CSU-X1 spinning-disk scan head and a Hamamatsu C9100-13 EMCCD camera. The entire system was controlled using Volocity software. Cells were imaged using a 100× oil-immersion CFI Plan Apochromat VC objective (1.4 NA, working distance 0.13 mm) with an optional 1.5× additional magnification. The second spinning-disk microscope consists of a Zeiss Axio Observer Z1 inverted stand attached to a Yokogawa CSU-W1 spinning-disk scan head and a Photometrics Prime BSI Scientific CMOS detector. Cells were imaged using 63× oil-immersion Plan Apochromat (1.4 NA, working distance 0.19 mm) and 100× oil-immersion Plan Apochromat (1.4 NA, working distance 0.17 mm) objectives combined with an optional 1.5× additional magnification. The LSM880 is an inverted laser-scanning confocal microscope with an Axio Observer stand. Cells were imaged using a 63× oil-immersion Plan Apochromat objective (1.4 NA, working distance 0.19 mm) and the Airyscan[46] detector. Acquisition on the latter systems is controlled via the Zen software (Zeiss). In all cases, samples were illuminated with 488 nm (mNeonGreen or GFP) and 561 nm (mCherry) lasers and appropriate fluorescence filter sets for these fluorophores. Photoconversion of mEOS3.2 was carried out using a 405-nm laser, with the non-converted state imaged using a 488-nm laser and the same filter set as for mNeonGreen/GFP, and the converted state imaged using a 561-nm laser and the same filter set as for mCherry. For regular live imaging on all systems, asynchronous cells were usually imaged using a 4.3 μm *Z*-stack with 16 slices at 270-nm vertical intervals, and time intervals ranging from 5 s to 120 s, never exceeding 30 min of continuous imaging. For Airyscan imaging, cells were imaged using a larger *Z*-stack at single time points. For SRRF and Hough fitting, cells were imaged with the system held at a single *Z*-plane and the imaging rate was increased to yield final reconstructed SRRF images at >3 frames per second. Instant SIM (iSIM) images were acquired with a Visitech VT-iSIM module and Hamamatsu Flash4.0 v.3 scientific CMOS camera, attached to an inverted Nikon TiE

microscope stand with Perfect Focus System and motorised stage (100× oil-immersion 1.45 NA Plan Apo λ objective).

Image processing

All basic image processing (cropping, viewing stacks, scaling for visual presentation and producing maximum-intensity projections) was carried out in Fiji[47] (ImageJ[48]). All time-lapse images subjected to SRRF analysis were processed with NanoJ-LiveSRRF, the newest implementation of NanoJ-SRRF[49]. NanoJ-LiveSRRF is available on request and is expected to be available for download soon. NanoJ-SRRF is already released and available as open-source software for Fiji and ImageJ. Airyscan processing and iSIM 3D deconvolution were carried out using proprietary Zen (Zeiss) and Elements (Nikon) software, respectively.

Image denoising for fast-acquired data

Denoising (Fig. 3c, Extended Data Fig. 4b) was performed using the Noise2Noise image restoration technique[50] as implemented using the CSBDeep/CARE framework[51]. Three separate Noise2Noise models were trained independently for Alm1–mNeonGreen images, Les1–mNeonGreen images and Cut11–mCherry images. Training data comprised 2,000 pairs of intensity-normalized 64 × 64-pixel patches in two adjacent frames, randomly selected from across all acquired data sets for each model. Validation data comprised an additional 200 pairs of 64 × 64-pixel patches randomly selected and normalized via the same method. Each model was trained with the following network parameters: training loss = mean-squared error, UNet kernel size = 3 × 3, training steps per epoch = 200, training epochs = 100. Jupyter notebooks for network training and prediction and trained Noise2Noise models are available at https://github.com/superresolusian/local-NEB.

Statistics and reproducibility

Through this paper, the basic independent biological unit of comparison is the single cell (undergoing nuclear division). For experiments using light microscopy, biological repeats refer to cells drawn from two different cultures and plated separately; technical repeats refer to cells drawn from the same culture but plated separately, usually imaged on the same day. For high-resolution (in time or space) imaging of strains already analysed by conventional confocal imaging, we focused on collecting data from additional technical repeats. The number of cells indicated in the legends that accompany representative images is a conservative estimate of the

number of cells, across biological and technical repeats, at the same cell cycle stage. Special considerations apply for electron microscopy (see 'Correlative fluorescence microscopy and electron tomography'). Since cells for all experiments were cultured at 32 °C in rich YES growth medium, we were able to pool cells across technical and biological repeats, as well as different clones carrying the same deletion or fluorescent protein tag, for population-level analyses (See 'Analysis framework for single-cell trajectories' and 'Population-level analyses').

Analysis framework for single-cell trajectories

Analysis of single-cell trajectories was carried out using custom software written for the open-source platform Fiji[47]. This is available from https://github.com/superresolusian/local-NEB.

Regions of interest selection

Regions of interest (ROIs) containing dividing cells were manually selected in time-series data. Only division events that completed were selected for analysis (Extended Data Fig. 2a, 'Manually select ROIs', 'Extracted ROI'). A ROI devoid of nuclei over the whole timelapse was also selected for background subtraction of measured intensities.

Detecting divisions

Each ROI was maximum-intensity projected and this projection was then blurred, binarised, hole-filled and skeletonised using ImageJ1 'binary' functions in Fiji[47]. The longest path of the skeleton structure was assumed to correspond to the dividing nucleus, and the angle formed by this line-like path measured to be the division angle θ (Extended Data Fig. 2a, 'Determine division angle').

Circle detection

Within ROIs, nuclei were identified for each frame and their radii determined using a custom-written Fiji plugin implementing the circular Hough transform[52] (Extended Data Fig. 2a, 'Circle detection'; each coloured circle denotes a separate detected nucleus). For two-colour images, the mNeonGreen channel was used to identify nuclei owing to their superior signal-to-noise ratio, and these nuclei centroid coordinates were assumed to be the same across both channels. For NLS images, a Sobel filter was applied to extract the perimeters of the nuclei before performing the circular Hough transform.

Identification of dividing nucleus pairs

For all possible pairs of detected circles in the ROI, the angle between the circle centres was calculated. Circle pairs oriented at angles different from the division angle θ by more than 30° were rejected. For proteins distributed along the whole length of the bridge between the two daughter nuclei (for example, Les1 as shown in Fig. 1d), all candidate bridge paths in each ROI frame were identified by blurring, binarising, hole-filling and skeletonising the images (skeleton paths shown in Extended Data Fig. 2a, 'Path segmentation'). Paths of length < 3 pixels were rejected as these corresponded to isolated nuclei (for example, Extended Data Fig. 2a, 'Path segmentation', blue paths). The end points of the remaining paths were then checked against the coordinates of the remaining circle pairs. Paths without anchoring circle detections were rejected (for example, Extended Data Fig. 2a, 'Path segmentation', pink paths), as were any detected circles lacking an associated path (for example, Extended Data Fig. 2a, 'Circle detection', red circle). The final result for each frame was either that no division events were successfully detected, or two nuclei and joining path were detected (Extended Data Fig. 2a, 'Filter circles and paths satisfying selection criteria'). Following breakage of the bridge, there is no longer a continuous path between the daughter nuclei. In this case, for a detected circle pair at an appropriate angle we joined two paths, each with one endpoint anchored at one of the circles, with a straight line between the 'free' endpoints (Extended Data Fig. 2a, 'Filter circles and paths satisfying selection criteria', yellow dotted line). For proteins not continuously present along the whole length of the bridge (for example, NLS as shown in Fig. 1a), the path corresponding to the bridge location was defined as a straight line between the two daughter nucleus circle centres.

Definition of bridge and time points

The bridge was defined as the connection between the two daughter nuclei excluding any pixels within the nuclei perimeters. The initiation of division was defined as the first frame in which two distinct nuclei were successfully detected, and dumb-bell appearance was defined as the first frame where a bridge could be discerned (that is, the first time point where all path pixels were not contained by daughter nuclei). Nucleus separation distance was defined as the Euclidean distance between the centroids of the daughter nuclei.

Measurement of nuclear intensities

Nuclear intensities were the background-subtracted average intensities within the detected circles (Fig. 1b, 'Nucleus', Fig. 4b).

Measurement of bridge intensities

Total bridge intensity was the background-subtracted average intensity along the bridge path (Fig. 1b, 'Bridge', Fig. 3e, Extended Data Figs. 4a, 5h, 7d, 8f). In all cases, the path line width was set to 5 (that is, 2 pixels perpendicularly either side of the path) to account for the full thickness of the bridges.

Measurement of vertical displacement of nuclear envelope proteins

Circle detection and analysis was again performed using the circular Hough transform, but this time on whole frames (that is, no manually selected ROIs) so that all nuclei within a single time frame were detected. All data analysed had Cut11–mCherry as a reference protein in one channel and another nuclear envelope protein of interest in the second channel. For each nucleus, the difference in radius between the two channels was calculated (Extended Data Fig. 2c, e). SRRF processing was performed on images before radius measurement to increase resolution. As a control, Nup60 was labelled with a green-to-red photoconvertable fluorescent protein (mEOS3.2) and images were taken before and after photoconversion. These two channels were then analysed using the same pipeline as for the Cut11 two-colour strains to check that there were no systematic errors in radius measurement between red and green channels. The values obtained for various Nups provide a good match with a recent electron microscopy analysis of the *S. pombe* NPC[53], which also provided the estimate of the width of the lumen between inner and outer nuclear envelopes.

Spindle detection and breakpoint measurement

Spindles were segmented from ROIs in images containing fluorescently labelled tubulin (mCherry–Atb2) by blurring, binarisation, hole-filling and skeletonisation. The longest path of the skeleton was determined for each frame; the frame in which spindle breakage occurred was determined as the first frame where the maximum skeleton path length decreased by $\geq 25\%$ compared to the maximum skeleton path length measured across all previous frames.

Quantifying early bridge intensities

Normalized bridge intensity for early bridges (Extended Data Fig. 7c) was calculated as

$$I_{\text{bridge}} = \frac{I_{\text{bridge}}(f) - I_{\text{bg}}(f)}{I_{\text{nuc}}(f) - I_{\text{bg}}(f)}$$

where f is the first frame in a nuclear division sequence in which a bridge appears that has 1 μm ≤ bridge length ≤ 2μm; I_{bridge} (f) is the average intensity along the bridge length in frame f (with a linewidth of 3 pixels for averaging adjacent to the bridge axis); I_{bg} (f) is the average intensity of the image background in frame f; and I_{nuc} (f) is the average intensity of interphase nuclei in frame f.

Bridge numbers were as follows: Cut11, n = 19; Cut11-*les1Δ*, n = 27 (P = 0.0179, unpaired two-tailed t-test); Nup60, n = 44; Nup60- *les1Δ*, n = 102 (P = 0.0722, unpaired two-tailed t-test).

Data curation

Every detected nucleus division was manually checked to ensure that the correct nuclei had been identified, and ROIs containing false detections were excluded from analysis.

Manual quantification

The breakpoint analysis in Extended Data Fig. 7f was scored manually owing to the high error rates of identifying the precise site of breakage from automatically extracted time-series data. The timings in Extended Data Fig. 6e–g (with reference to the first appearance of the nuclear bridge) were manually quantified. This was due to the presence of a second green label (Cdc15–mNeonGreen) in addition to Cut11–GFP; while this allowed the visualization of the cytokinetic ring, it also prevented the automated analysis of maximum-intensity projections.

Population-level analyses

Unless otherwise specified, single-cell trajectories (see ‘Manual quantification’ for specific exceptions [Author: Please specify which section you mean.]) were aligned to the time of maximal spindle elongation (if a tubulin label was not present, measured indirectly using the maximal separation between daughter nuclei as a proxy for spindle length)—making use of the fact that spindle elongation kinetics are highly reproducible from cell to cell. When combining trajectories from different strains (for example, Fig. 3e), we made use of the observation that

mitotic timing tends to be consistent even when spindles reach different maximum lengths (Extended Data Fig. 5b). This is probably owing to a Klp9-dependent adjustment in spindle elongation rates between strains (strains with longer spindles elongate their spindles faster)[17]. Statistical analyses were carried out using GraphPad (mean and standard deviation of averaged traces), MATLAB (ANOVA; mean and standard deviation of averaged traces) and the Estimation Stats platform[54] (two-sided Mann–Whitney). Graphs and heat maps were generated using either GraphPad or MATLAB.

Correlative fluorescence microscopy and electron tomography

Correlative microscopy was done as described before for resin-embedded yeast cells[55,56], with minor modifications. In brief, Les1–mNeonGreen/mCherry–Atb2-expressing cells and Cut11–GFP/mCherry–AHDL-expressing *les1Δ* cells were grown in YES at 32 °C to mid-log phase, pelleted by vacuum-filtration and high-pressure frozen in the 100 µm recess of aluminium carriers (Wohlwend) using an HPM100 (Leica Microsystems). Samples were freeze-substituted and embedded in Lowicryl HM20 (Polysciences) according to the published protocol[55], except with 0.03% uranyl acetate in the freeze-substitution solution, and for the *les1Δ* experiment, samples were shaken on dry ice for 2 h during freeze-substitution. Resin blocks were sectioned at 320-nm nominal thickness, picked up onto carbon-coated copper grids (AGS160, Agar Scientific) and imaged on the same day on a Nikon TE2000 or Ti2 microscope using a 100× TIRF objective, a NEO sCMOS DC-152Q-C00-FI camera (Andor), and a Niji LED light source. Based on the fluorescence images, cells with profiles in which an elongated bridge was visible within the section plane were selected for electron tomography. Protein A-coated gold 15-nm beads (EMS) were adhered to the grids before Reynolds' lead citrate staining. Dual-axis electron tomographic tilt series were acquired approximately from +60° to −60° on a TF20 electron microscope (FEI) operated in STEM mode, using a 50 µm C2 aperture, at 1° increment and 1.1-nm pixel size on an axial bright field detector[57], using SerialEM[58]. Both wild type and *les1Δ* data are each from one high-pressure freezing and freeze-substitution experiment. Tomograms were reconstructed using IMOD[59]. Segmentation models were generated using Amira (Thermo Fisher Scientific) by manual tracing of membranes and microtubules, followed by extensive simplification and smoothening of the generated surfaces. Therefore, segmentation models are for purely illustrative purposes. Segmentation models are inverted in z or rotated around x or y relative to the original tomograms, thus the corresponding electron tomographic slices in figure

panels Fig. 2b, c, Extended Data Fig. 3c are shown flipped relative to the original tomograms. Some of the electron tomographic slices shown in figures have been mildly gauss-filtered to improve visibility. NPC nearest neighbour distances were measured in IMOD[59]. An IMOD model file was manually generated of the centres of all visible nuclear pores, and the programme imod-dist was used to obtain distances of each pore to all other pores. For each nuclear pore, the shortest distance was determined to be the distance to its nearest neighbour.

Reporting summary

Further information on research design is available in the Nature Research Reporting Summary linked to this paper.

Data availability

Bulk microscopy time-series data, comprising more than 50 files with an average size over 1 GB, are available upon request. The *S. pombe* strains generated for and used in this study (Extended Data Table 1) are available upon request.

Code availability

All custom software designed for and used in this study is freely available on GitHub in a public repository at https://github.com/superresolusian/local-NEB. The use of this code is governed by an MIT license.

<jrn>29. Yang, J. et al. The I-TASSER suite: protein structure and function prediction. *Nat. Methods* **12**, 7–8 (2015). Medline CrossRef</jrn>

<jrn>30. Roy, A., Kucukural, A. & Zhang, Y. I-TASSER: a unified platform for automated protein structure and function prediction. *Nat. Protoc.* **5**, 725–738 (2010). Medline CrossRef</jrn>

<jrn>31. Eddy, S. R. Accelerated profile HMM searches. *PLOS Comput. Biol.* **7**, e1002195 (2011). Medline CrossRef</jrn>

<jrn>32. Katoh, K., Misawa, K., Kuma, K. & Miyata, T. MAFFT: a novel method for rapid multiple sequence alignment based on fast Fourier transform. *Nucleic Acids Res.* **30**, 3059–3066 (2002). Medline CrossRef</jrn>

<jrn>33. Katoh, K., Rozewicki, J. & Yamada, K. D. MAFFT online service: multiple sequence alignment, interactive sequence choice and visualization. *Brief. Bioinform.* **20**, 1160–1166 (2019). Medline CrossRef</jrn>

<jrn>34. Capella-Gutiérrez, S., Silla-Martínez, J. M. & Gabaldón, T. trimAl: a tool for automated alignment trimming in large-scale phylogenetic analyses. *Bioinformatics* **25**, 1972–1973 (2009). Medline CrossRef</jrn>

<jrn>35. Nguyen, L.-T., Schmidt, H. A., von Haeseler, A. & Minh, B. Q. IQ-TREE: a fast and effective stochastic algorithm for estimating maximum-likelihood phylogenies. *Mol. Biol. Evol.* **32**, 268–274 (2015). Medline CrossRef</jrn>

<jrn>36. Kalyaanamoorthy, S., Minh, B. Q., Wong, T. K. F., von Haeseler, A. & Jermiin, L. S. ModelFinder: fast model selection for accurate phylogenetic estimates. *Nat. Methods* **14**, 587–589 (2017). Medline CrossRef</jrn>

<jrn>37. Finn, R. D. et al. Pfam: the protein families database. *Nucleic Acids Res.* **42**, D222–D230 (2014). Medline CrossRef</jrn>

<jrn>38. El-Gebali, S. et al. The Pfam protein families database in 2019. *Nucleic Acids Res.* **47** (D1), D427–D432 (2019). Medline CrossRef</jrn>

<jrn>39. Robert, X. & Gouet, P. Deciphering key features in protein structures with the new ENDscript server. *Nucleic Acids Res.* **42**, W320–W324 (2014). Medline CrossRef</jrn>

<jrn>40. Forsburg, S. L. & Rhind, N. Basic methods for fission yeast. *Yeast* **23**, 173–183 (2006). Medline CrossRef</jrn>

<jrn>41. Moreno, S., Klar, A. & Nurse, P. Molecular genetic analysis of fission yeast *Schizosaccharomyces pombe*. *Methods Enzymol.* **194**, 795–823 (1991). Medline CrossRef</jrn>

<jrn>42. Bähler, J. et al. Heterologous modules for efficient and versatile PCR-based gene targeting in *Schizosaccharomyces pombe*. *Yeast* **14**, 943–951 (1998). Medline CrossRef</jrn>

<jrn>43. Murray, J. M., Watson, A. T. & Carr, A. M. Transformation of *Schizosaccharomyces pombe*: lithium acetate/ dimethyl sulfoxide procedure. *Cold Spring Harb. Protoc.* **2016**, pdb.prot090969 (2016). Medline CrossRef</jrn>

<jrn>44. Zhang, M. et al. Rational design of true monomeric and bright photoactivatable fluorescent proteins. *Nat. Methods* **9**, 727–729 (2012). Medline CrossRef</jrn>

<jrn>45. Escorcia, W. & Forsburg, S. L. Tetrad dissection in fission yeast. *Methods Mol. Biol.* **1721**, 179–187 (2018). </jrn>

<jrn>46. Huff, J. et al. The new 2D superresolution mode for ZEISS Airyscan. *Nat. Methods* **14**, 1223 (2017). CrossRef</jrn>

<jrn>47. Schindelin, J. et al. Fiji: an open-source platform for biological-image analysis. *Nat. Methods* **9**, 676–682 (2012). Medline CrossRef</jrn>

<jrn>48. Schneider, C. A., Rasband, W. S. & Eliceiri, K. W. NIH Image to ImageJ: 25 years of image analysis. *Nat. Methods* **9**, 671–675 (2012). Medline CrossRef</jrn>

<jrn>49. Gustafsson, N. et al. Fast live-cell conventional fluorophore nanoscopy with ImageJ through super-resolution radial fluctuations. *Nat. Commun.* **7**, 12471 (2016). Medline CrossRef</jrn>

<conf>50. Lehtinen, J. et al. Noise2Noise: learning image restoration without clean data. In *35th Int. Conf. Mach. Learn.* **7**, 4620–4631 (2018).</conf>

<jrn>51. Weigert, M. et al. Content-aware image restoration: pushing the limits of fluorescence microscopy. *Nat. Methods* **15**, 1090–1097 (2018). Medline CrossRef</jrn>

<jrn>52. Ballard, D. H. Generalizing the Hough transform to detect arbitrary shapes. *Pattern Recognit.* **13**, 111–122 (1981). CrossRef</jrn>

<jrn>53. Asakawa, H. et al. Asymmetrical localization of Nup107–160 subcomplex components within the nuclear pore complex in fission yeast. *PLoS Genet.* **15**, e1008061 (2019). Medline CrossRef</jrn>

<jrn>54. Ho, J., Tumkaya, T., Aryal, S., Choi, H. & Claridge-Chang, A. Moving beyond *P* values: data analysis with estimation graphics. *Nat. Methods* **16**, 565–566 (2019). Medline CrossRef</jrn>

<jrn>55. Kukulski, W. et al. Precise, correlated fluorescence microscopy and electron tomography of lowicryl sections using fluorescent fiducial markers. *Methods Cell Biol.* **111**, 235–257 (2012). Medline CrossRef</jrn>

<jrn>56. Bharat, T. A. M., Hoffmann, P. C. & Kukulski, W. Correlative microscopy of vitreous sections provides insights into BAR-domain organization in situ. *Structure* **26**, 879–886 (2018). Medline CrossRef</jrn>

<jrn>57. Hohmann-Marriott, M. F. et al. Nanoscale 3D cellular imaging by axial scanning transmission electron tomography. *Nat. Methods* **6**, 729–731 (2009). Medline CrossRef</jrn>

<jrn>58. Mastronarde, D. N. Automated electron microscope tomography using robust prediction of specimen movements. *J. Struct. Biol.* **152**, 36–51 (2005). Medline CrossRef</jrn>

<jrn>59. Kremer, J. R., Mastronarde, D. N. & McIntosh, J. R. Computer visualization of three-dimensional image data using IMOD. *J. Struct. Biol.* **116**, 71–76 (1996). Medline CrossRef</jrn>

Acknowledgements We thank M. Balasubramanian, S. Oliferenko, S. Hauf, K. Gould, J. Bahler, P. Nurse and their laboratories for sharing *S. pombe* strains, plasmids, expertise and *S. pombe* protocols; J. O. Patterson for the gift of pFA6a-mNeonGreen plasmids; the LMB electron microscopy facility for electron microscopy support; T.-O. Buchholz for advice on the Noise2Noise implementation.; and D. Albrecht, I. Raote, A. Chaigne, P. Pereira, C. Jacobs and members of the Baum laboratory, in particular G. Paci, G. Cazzagon and H. Matthews, for their feedback on this manuscript. G.D. was funded by a European Union Marie Sklodowska-Curie Individual Fellowship (704281-CCDSA) and the Wellcome Trust (203276/Z/16/Z). Siân C. and R.H. were supported by the UK Biotechnology and Biological Sciences Research Council (BB/R021805/1; BB/S507532/1), the UK Medical Research Council (MR/K015826/1) and the Wellcome Trust (203276/Z/16/Z). Scott C. was supported by the Francis Crick Institute, which receives its core funding from Cancer Research UK (FC001121), the UK Medical Research Council (FC001121) and the Wellcome Trust (FC001121). W.K. was funded by the Medical Research Council (MC_UP_1201/8). B.B. was supported by UCL's Institute for the Physics of Living Systems, the MRC-LMCB, the Wellcome Trust (203276/Z/16/Z) and Cancer Research UK (C1529/A28276).[Author: Please note that we are not allowed to thank reviewers in this section – this is covered by 'Peer review information' below.]

Author contributions G.D. co-conceived the project, designed and implemented all the experiments, generated strains and reagents, acquired, analysed and interpreted the data (with the exception of the electron microscopy data shown in parts of Figs. 2, 4, Extended Data Figs. 3, 7, and led the drafting of the paper. Siân C. and U.S. created new software used in the work, and analysed and assisted in the interpretation of data. Scott C. advised on experimental design, helped to generate strains and reagents, and provided protocols and training. R.H. advised on the creation of new software used for the project. W.K. performed all electron tomography and analysis of electron tomograms (parts of Figs 2, 4, Extended Data Figs. 3, 7). B.B. co-conceived and supervised the project, provided advice on experimental design, implementation and analysis and co-drafted the manuscript. All authors provided input during the manuscript drafting stage.

Competing interests The authors declare no competing interests.

Additional Information

Supplementary information is available for this paper at

Correspondence and requests for materials should be addressed to G.D. or B.B.

Peer review information *Nature* thanks Brian Burke and the other, anonymous, reviewer(s) for their contribution to the peer review of this work.

Reprints and permissions information is available at http://www.nature.com/reprints.

[Author: Please ensure that the following information is included in the figure legends where relevant. Sample size (exact *n* number); a statement of replicability (how many times was experiment replicated in the lab); description of sample collection (clarify whether technical or biological replicates and include how many animals, litters, cultures, etc.); state the statistical test used and give *P* values; define centre values (median or average) and error bars. For figures/images that are reproduced or adapted from a third party, it is important that you confirm that permission has been obtained and that appropriate acknowledgement of the copyright holder is given.]

Extended Data Fig. 1 | ER topology; Les1 structure and phylogeny. a, Airyscan reconstructions of cells expressing the mCherry-AHDL synthetic construct. Orange arrows indicate tubules linking the outer nuclear envelope to the cortical ER. Purple arrows indicate the displacement of the cortical ER by the division ring (not shown). The blue bar indicates the central ER plate formed during late anaphase. Representative of more than 20 cells across 3 technical repeats. Scale bar = 2 μm. **b**, Genome-wide genetic interaction scores (E-MAP) with Les1/SPAC23C4.05c. Data from Frost et al. 2012. **c**, Schematic representation of Les1 sequence

with positions of conserved motifs indicated. **d**, Phylogenetic tree of Les1 homologues across *Schizosaccharomyces* species with single *S. cerevisiae* homologue MSC1 grouping separately, indicating a duplication in the lineage leading up to *Schizosaccharomyces*. Bootstrap values indicated at nodes. See Methods for details of tree construction. **e**, Alignment of Les1 homologues with key conserved motifs highlighted. Colour-coded by % similarity. See Methods for details.

Extended Data Fig. 2 | Image analysis workflow and its application to NE protein localization and spindle breakdown timings. a, Schematic demonstrating pipeline for detecting and measuring nuclei and bridges in time-lapse data. Individual steps are described fully in the Methods. Representative images shown here are of Les1-mNeonGreen and Atb2-mCherry. **b**, The delay between reaching maximum spindle length (spindle max.) and spindle breakage, in seconds. Spindle breakage always follows maximal extension. Sample size(n) = 39 individual cells drawn from 3 biological repeats of the entire experiment. Central line represents the mean and the error bars represent the standard deviation of the population. **c**, Images of two-colour strains used for relative localization of nuclear envelope and NPC components and nucleus radii (r) as measured using the circular Hough transform, representative of more than 130 individual cells each drawn from 2 biological repeats. **d**, **e**, The vertical displacement (relative to the plane of the nuclear envelope) of various nuclear pore complex components (**e**) (schematised in **d**; Nup60, in the nuclear ring; Alm1 and Nup211 in the basket; transmembrane Nup Pom34) and nuclear envelope (NE) membrane proteins (Cta4) relative to Cut11. These measurements correspond to the differences in r as shown in **c**. Nup60-mEOS was used as an internal control, with the values representing the displacement of photo-converted Nup60-mEOS (red channel) relative to un-converted Nup60-mEOS (green channel). The dotted lines represent an estimate of the thickness of the nuclear envelope (see Methods for details). *n* = 393 (Cta4), 455 (Pom34), 266 (Les1), 185 (Nup60), 280 (Nup211), 218 (Alm1), and 135 (Nup60-mEOS) individual cells, each drawn from across 2 biological repeats of the entire experiment. The measure of centre (central line) shows the mean of each population and the error bars represent the standard deviation.

Extended Data Fig. 3 | Electron tomography of mid- and early-stage bridges with correlative fluorescence images. a, Fluorescence images of resin sections through cells expressing Les1-mNeonGreen (green) and Atb2-mCherry (magenta), corresponding to cells that

were imaged by electron tomography and are shown in Fig. 2b (left image), Fig. 2c top panel (middle image) and Fig. 2c lower panel (right image). Images have been rotated to match approximately the orientation of electron tomograms. Scale bars = 1 μm. Representative of 1 (Fig. 2b) and 5 technical repeats (Fig. 2c), respectively. **b**, Fluorescence image of resin section through a cell expressing Les1-mNeonGreen (green) and Atb2-mCherry (magenta), corresponding to cell imaged by electron tomography shown to the right, indicated by white region. Scale bar = 1 μm. The right two panels are virtual slices through electron tomograms of the cell shown to the left. The approximate overlap in field of view of the tomograms is indicated by dashed lines. Note that no NPCs are visible in the stalk part shown in top image. NPCs (indicated by blue arrowheads) are constrained to the midzone (bottom image). Scale bars = 100 nm. Representative of 2 technical repeats. **c**, Early stage bridge of a dividing cell; same electron tomogram and cell as shown in Fig. 2b. Top panel is the segmentation model; white area corresponds to the panels below. Inset slice 1 is a virtual slice through the electron tomogram showing the centres of microtubules, indicated by white arrowheads. Inset slice 2 is 18 nm apart in z and shows a nuclear pore, indicated by blue arrowheads. The NPC thus projects less than 18 nm into the nucleoplasm before encountering the microtubules. 1 technical repeat. Scale bars = 50 nm.

Extended Data Fig. 4 | Dynamics of individual nucleoporins. a, Averaged normalized intensity traces for Alm1-mNeonGreen (between 9 cells at t = -300 to 26 cells at t = 0) aligned by spindle max (t = 0). The central line represents the mean of the population; the shaded area depicts the standard deviation. Images on right are confocal maximum intensity projections of dividing cells expressing Alm1-mNeonGreen and Cut11-mCherry, representative of more than 20 cells across 3 biological repeats. Scale bar = 2 μm. **b**, Kymograph of intensities averaged across a single confocal plane of a dividing cell expressing Cut11-mCherry and Alm1-mNeonGreen and imaged at 3 frames per second followed by denoising (see Methods). Representative of more than 10 cells across 2 technical repeats. **c**, Confocal maximum intensity projections of dividing cells expressing Nup211-mNeonGreen and Cut11-mCherry. Representative of more than 30 cells across 3 biological repeats. Scale bar = 2 μm. **d**, Schematic indicating effect of deleting Nem1 on nuclear envelope surface area and tension. **e**, Confocal maximum intensity projections of *nem1*Δ cells expressing Nup211-mNeonGreen and Cut11-mCherry. Representative of more than 30 cells across 2 biological repeats. Scale bar = 2 μm.

Note that the basket Nup is able to enter the nuclear bridge in this condition. **f**, Confocal maximum intensity projections of dividing cells expressing various NPC subcomplex components tagged with mNeonGreen at their C termini, co-expressed in each case with Cut11-mCherry. Each set of panels is representative of >20 cells across 2 biological repeats. Scale bars = 2 μm.

Extended Data Fig. 5 | Relative localization of Les1 and nucleoporins. a, Averaged line traces (darker lines = mean, lighter bands = standard deviation) of Les1 and Cut11 intensities along the bridge for 16 cells aligned at bridge length 3 μm. **b**, Time from bridge formation to maximum spindle length measured for strains pooled to generate Fig. 3g (GD173, GD250) and S4d (GD176, GD253). Numbers in brackets (n) indicate number of cells in each population, with bars representing mean and standard deviation. The ANOVA F statistic and p-value are listed above each plot. The line and pairwise p-value within each plot refer to the comparison between pooled strains. **c**, Single Airyscan reconstructions of cells expressing Cut11 tagged at the endogenous locus with mNeonGreen and a synthetic mCherry-AHDL construct. Magenta arrow highlights stray nuclear pore cluster accompanied by widening of the nuclear envelope. Representative of more than 10 cells across 2 technical replicates. Scale bar = 2 μm. **d**, Maximum intensity projections of confocal images acquired every 60 s of cells expressing Les1-mNeonGreen and Cut11-mCherry. Bridge formation is at $t = 0$. Green arrows mark boundaries of Les1 stalks, magenta arrow indicates stray pore cluster. Representative of more than 50 cells across 6 biological repeats. Scale bar = 2 μm. **e**, SRRF reconstruction from single confocal planes of a cell expressing Les1-mNeonGreen and Cut11-mCherry. Magenta arrow indicates stray nuclear pore cluster, with examples marked upon the line scans along the bridges of 3 illustrative cells in **f**, Representative of more than 20 cells across 4 biological repeats. **g**, Confocal maximum intensity projections of cells expressing Cut11-GFP and Atb2-mCherry and acquired at 10 s intervals. Scale bars = 2 μm. Representative of more than 20 cells across 2 biological repeats. **h**, Relative NPC decay rates, calculated for a strain expressing both Nup60 and Cut11 (GD173; between 11 cells at $t = -300$ and 34 cells at $t = 0$), showing similar relative rates to a cross-strain comparison, as in **b** or Fig. 3g. Line shows mean of the population. **i**, Kymograph generated using 10 fps single plane imaging of a strain expressing Nup60 and Cut11 tagged at the endogenous loci with mNeonGreen and mCherry respectively. Blue (Nup60) and

magenta (Cut11) arrows represent the staggered decay of individual clusters of nuclear pores. Representative of more than 10 cells drawn from 2 technical replicates.

Extended Data Fig. 6 | Response of nuclear division dynamics to acute perturbations. a, Confocal maximum intensity projections of *nem1*Δ cells expressing Les1-mNeonGreen and Cut11-mCherry. Note the absence of Les1 stalk formation. Schematic indicates opposing effects of *nem1*Δ and Cerulenin treatment. Representative of more than 30 cells drawn from 2 biological repeats. Scale bar = 2 μm. **b**, Two examples of nuclei attempting to divide in the presence of 10 μM Cerulenin. Note Les1 stalk formation along aberrant bridge-like projections. Magenta arrows indicate NPC clusters. Representative of more than 30 cells drawn from 3 biological repeats. **c**, Dividing cells expressing the Ark1-as3 analogue-sensitive allele, either co-expressing Les1-mNeonGreen and mCherry-Atb2 or Les1-mNeonGreen and Cut11-mCherry and treated with 5 nM 1NM-PP1 and 5 μM Latrunculin A. In both cases, representative of more than 30 cells across 2 biological repeats. Scale bars = 2 μm. **d**, iSIM image of *imp1*Δ cells expressing Les1-mNeonGreen and Cut11-mCherry. Arrows highlight isolated NPC clusters in Les1-depleted regions. Representative of more than 40 cells across 2 biological replicates. Scale bar = 2 μm. **e**, Time-lapse confocal images of cells expressing Cut11-GFP, Cdc15-mNeonGreen, and mCherry-AHDL acquired at 60 s intervals with frames displayed at 3-min intervals. Representative of more than 50 cells across 3 biological replicates. Scale bars = 4 μm. **f**, Treatment with Latrunculin A depolymerizes the actin ring (marked by Cdc15) but has a minimal impact on the time of nuclear division, as marked by the time from bridge formation to complete NPC signal loss. Numbers above and below the horizontal bar represent the difference in means with 95% confidence interval and the two-sided Mann–Whitney p-value. n = 180 (untreated) and 146 (Lat A) individual cells in each population, in each case pooled from 3 biological replicates. Overlaid on individual data points, the upper and lower extent of the boxes span the inter-quartile range and the central bar denotes the median. **g**, Cytokinetic ring constriction only begins after nuclear division completes, and it takes almost 30 min for the ring to constrict and septation to complete. n = 222 (NPC loss to constriction start), 103 (constriction start to end) and 111 (constriction end to septation) individual cells in each population, in each case pooled from 3 biological replicates. Overlaid on individual data points, the upper and lower extent of the boxes span the inter-quartile range and the central bar denotes the median.

Extended Data Fig. 7 | Nucleoporin localization and dynamics in *les1Δ* cells. **a**, Fluorescence image of resin section through a *les1Δ* cell expressing Cut11-GFP (green) and a synthetic mCherry-AHDL construct (magenta), corresponding to the cell that was imaged by electron tomography shown in Fig. 4c. Representative of 2 technical repeats. Scale bar = 1 μm. **b**, Inter-pore distances for tomograms shown in Supplementary Figs. 2b (WT Early stage), 3b (WT Mid-stage), and tomogram not shown (*les1*Δ Mid-stage). See Methods for details on measurement. *n* = 26 (WT mid-stage), 18 (WT early stage) and 18 (*les1*Δ mid-stage) individual nuclear pores in each data set. The central lines represent the mean of the population, with the error bars representing standard deviation. **c**, Bridge intensity at bridge formation as an indirect readout of nucleoporin copy number in individual cells, for wild-type (WT) and *les1*Δ cells. *n* = 19 (WT Cut11), 27 (*les1*Δ Cut11), 44 (WT Nup60) and 102 (*les1*Δ Nup60) individual cells pooled from a minimum of 2 biological replicates. Bars overlaid on top of individual data points represent the mean (central line) and standard deviation (error bars). p-values derive from a two-tailed unpaired *t*-test. See Methods for details. **d**, Decay curves for NLS-GFP (orange, from 28 cells at *t* = -300 to 39 cells at *t* = 0), Nup60 (blue, from 10 cells at *t* = -300 to 15 cells at *t* = 0) and Cut11 (magenta, from 10 cells at *t* = -300 to 15 cells at *t* = 0) in a *les1*Δ background, drawn from a minimum of 2 biological replicates. Each trace was normalized by division by maximum bridge signal for that cell before averaging. The plot on the left represents the population averages for each marker in a *les1*Δ background, and the dotted orange line indicates exponential fit to the NLS-GFP average. The 3 subsequent plots show the averages (darker line) and standard deviation (shaded area) for each marker (NLS-GFP, orange; Nup60, blue; Cut11, magenta) in a *les1*Δ background, overlaid on the wild-type equivalents in grey. **e**, *les1*Δ cells expressing Alm1-mNeonGreen and Cut11-mCherry. Arrow indicates a small cluster of Alm1 that enters the bridge but then disappears. Representative of more than 20 cells from 2 biological repeats. Scale bar = 2 μm. f. SRRF reconstructions of confocal slices at 28 s intervals of *les1*Δ cells expressing Nup60-mNeonGreen and Cut11-mCherry tagged at the endogenous loci, aligned relative to spindle max (*t* = 0). Representative of more than 10 cells across 2 technical replicates. Magenta arrow indicates breakpoint. Scale bar = 2 μm. On the right, the cumulative distribution (42 cells from 2 strains across 3 biological replicates) of breakpoint locations relative to the midzone in *les1*Δ cells. The shaded grey area represents the mean +/− standard deviation of breakpoint locations in

wild-type cells (31 cells from 2 biological replicates), with the cumulative distribution as a grey line.

Extended Data Fig. 8 | Les1 truncations and genetic interactions. a, Schematic indicating Les1 truncation constructs, with numbers representing amino acid positions starting from 1 at the N terminus. Lower panels, cells expressing Les1 (1-291)-mNeonGreen, replacing Les1 at the endogenous locus, as well as Cut11-mCherry. See Methods for details on the truncation constructs (all at endogenous locus, replacing endogenous copy). Note the absence of detectable stalks and the delocalization of Cut11 in the bridge. Representative of more than 10 cells across 2 biological repeats. Scale bar = 5 μm. **b**, Confocal maximum intensity projections of cells expressing Cmp7-mNeonGreen and Les1-mScarlet. Arrows indicate Cmp7 foci at the tips of retracting stalks. Representative of more than 20 cells across 4 biological repeats. Scale bar = 2 μm. **c**, Single iSIM slice of a dividing cell expressing Cmp7-mNeonGreen and Les1-mScarlet, representative of more than 5 cells drawn from 2 technical repeats. Scale bar = 2 μm. **d**, Tetrad dissection assay for *les1*Δ crossed with either *lem2*Δ or *cmp7*Δ, showing colonies grown from individual spores. See Methods for details. **e**, Single image of double deletion strains, derived from the tetrad assay clones shown in **d**, expressing a synthetic NLS-GFP construct. Scale bar = 10 μm. Representative of more than 200 cells drawn from 2 biological repeats. **f**, Averaged line traces (darker lines = mean, lighter bands = standard deviation) of Nup60-mCherry intensities in *les1*Δ cells (grey: control; blue: treated with 10 μM Cerulenin) at bridge length 3 μm (n = 45 cells for cerulenin-treated; n = 27 cells for control). **g**, Confocal maximum intensity projections of *les1*Δ *lem2*Δ cells expressing Cut11-mCherry, either in the presence (lower panel) or absence (upper panel) of 5 μM Latrunculin A. Representative of more than 20 cells across 3 technical repeats. Scale bar = 2 μm.

Extended Data Table 1 | Complete list of *S. pombe* strains used in this study.
List of all the *Schizosaccharomyces pombe* strains used in this study along with their full genotypes and any relevant strain construction notes.

Publisher: NPG; Journal: Nature: Nature; Article Type: Biology article
MS nr: 2019-08-12893D

Figure 1

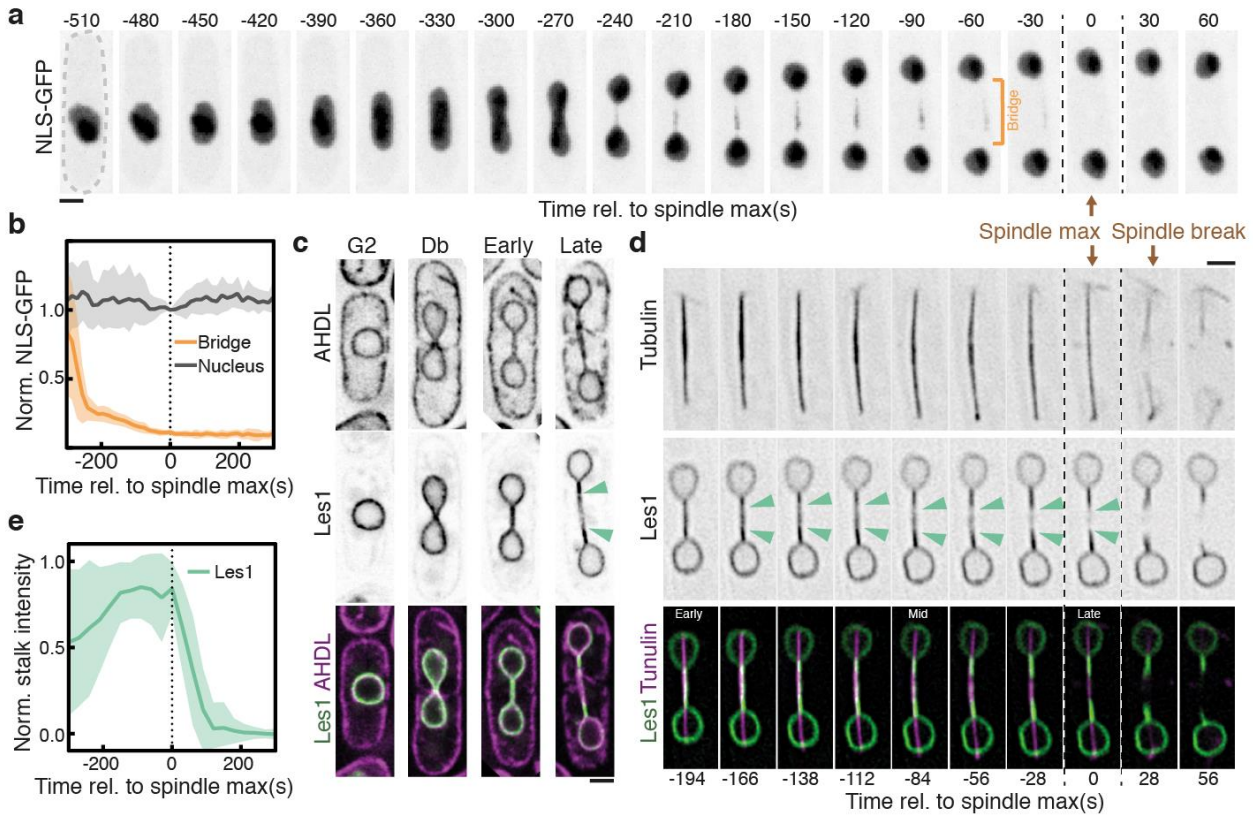

Figure 2

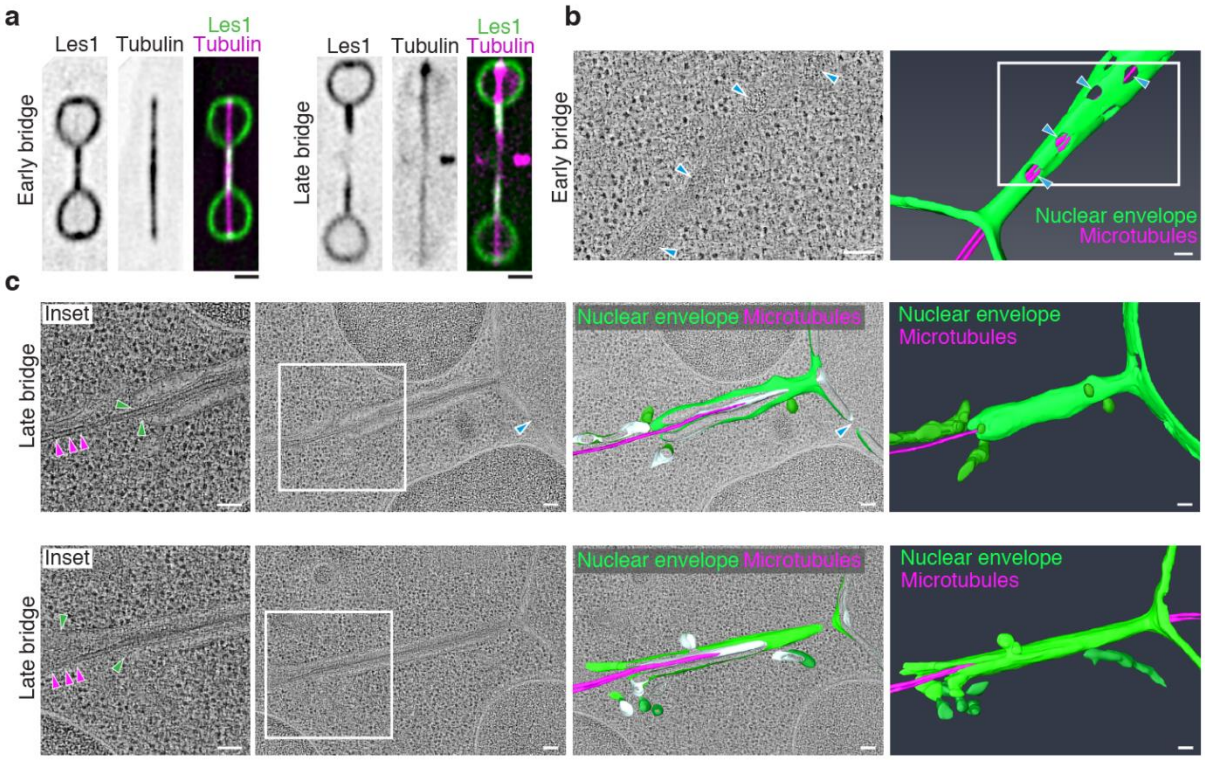
a
Les1
Tubulin
Les1
Tubulin
Early bridge
Les1
Tubulin
Les1
Tubulin
Late bridge
b
Early bridge
Nuclear envelope
Microtubules
c
Inset
Late bridge
Nuclear envelope Microtubules
Nuclear envelope
Microtubules
Inset
Late bridge
Nuclear envelope Microtubules
Nuclear envelope
Microtubules

Publisher: NPG; Journal: Nature: Nature; Article Type: Biology article
MS nr: 2019-08-12893D

Figure 3

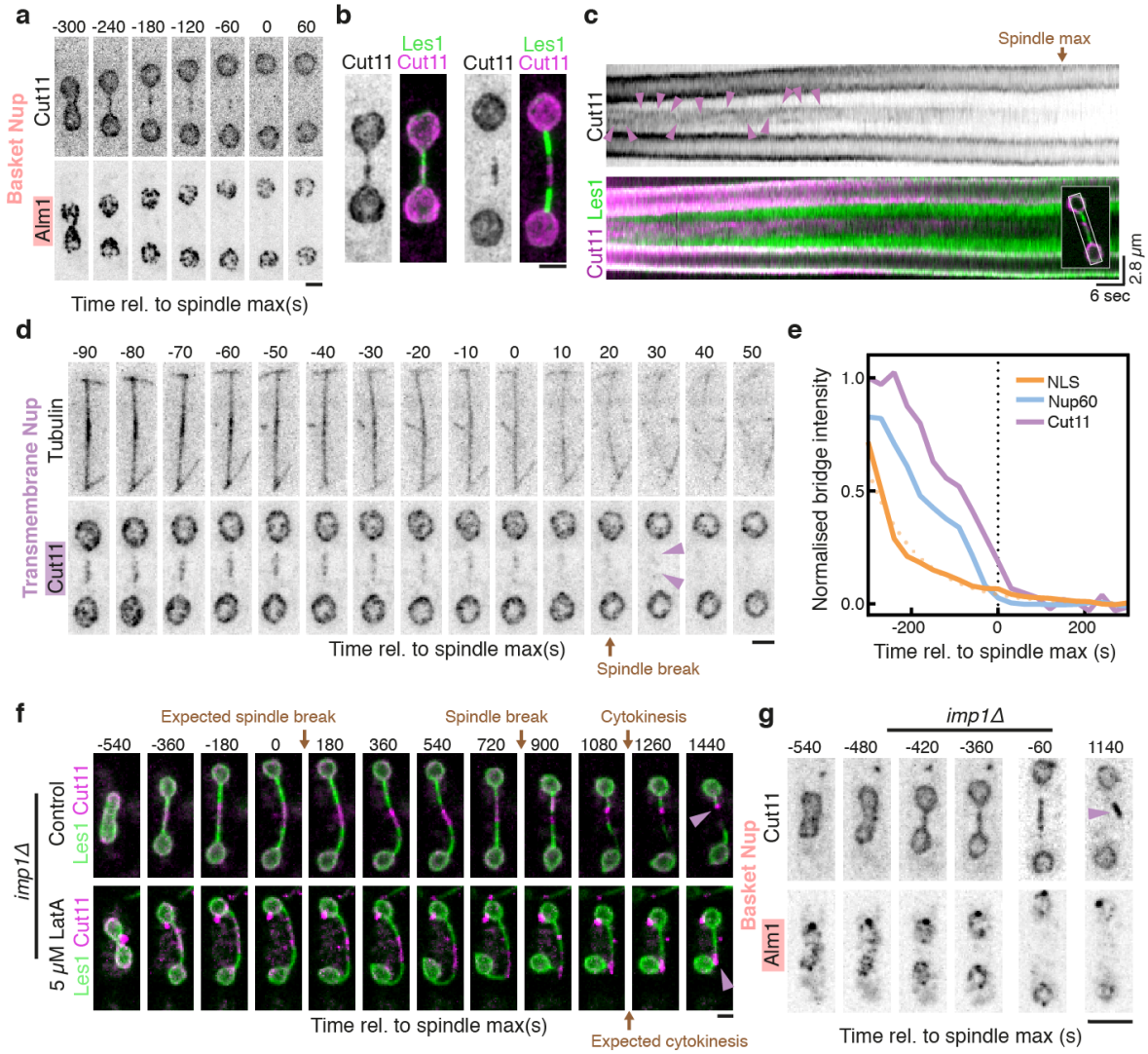

Publisher: NPG; Journal: Nature: Nature; Article Type: Biology article
MS nr: 2019-08-12893D

Figure 4

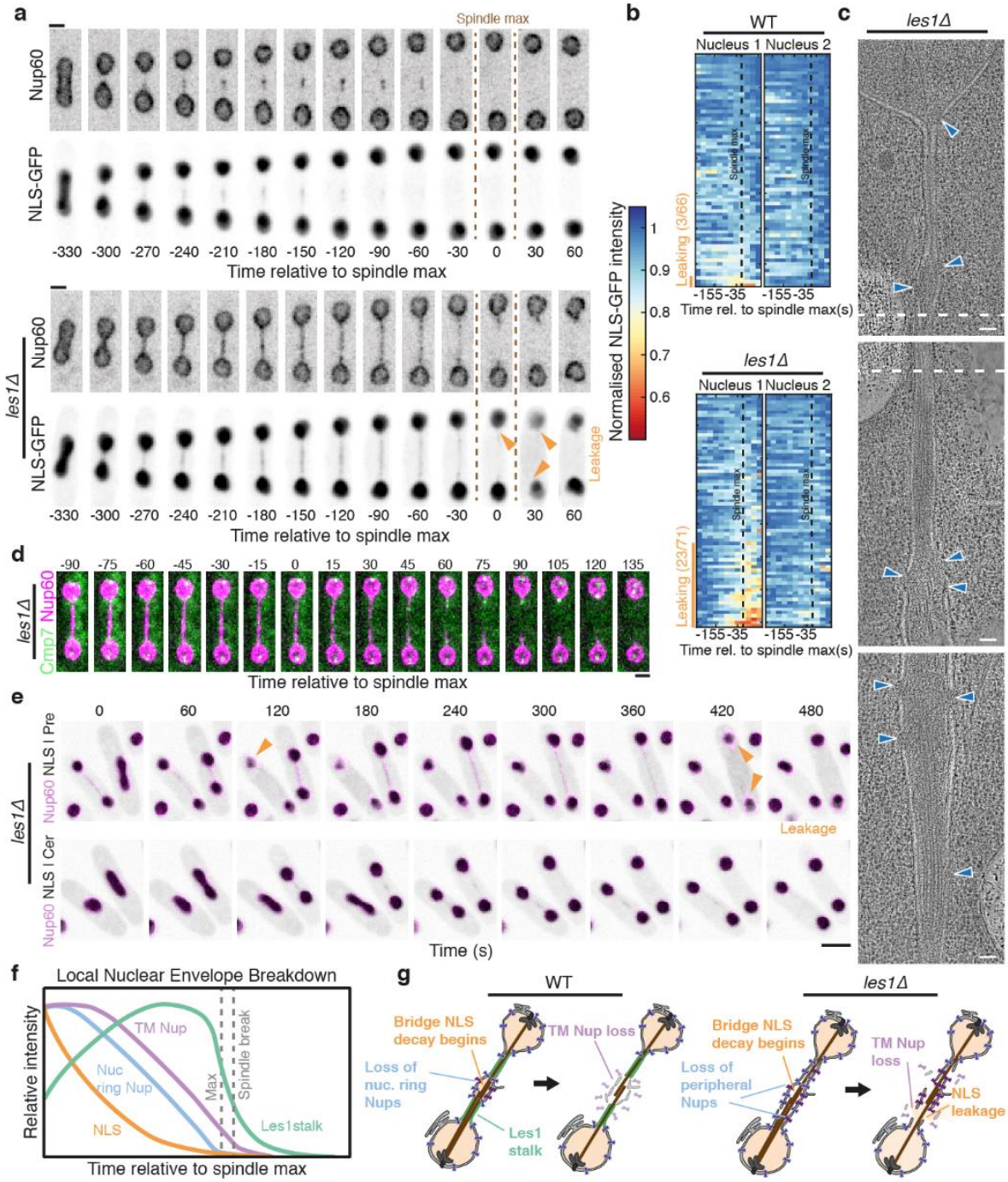

Extended Data Figure 1

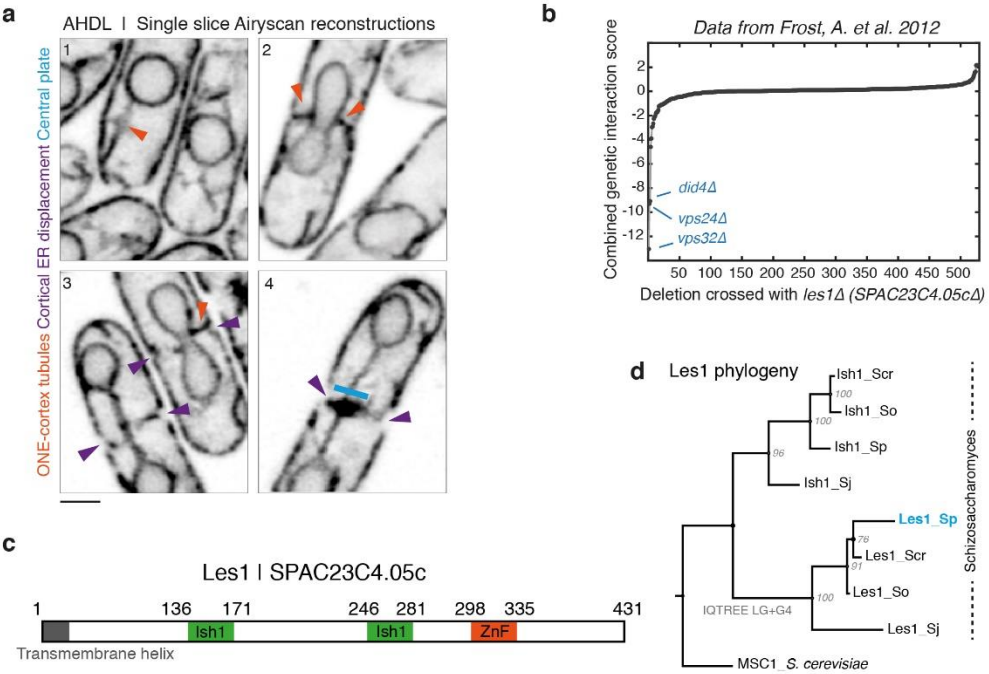

e

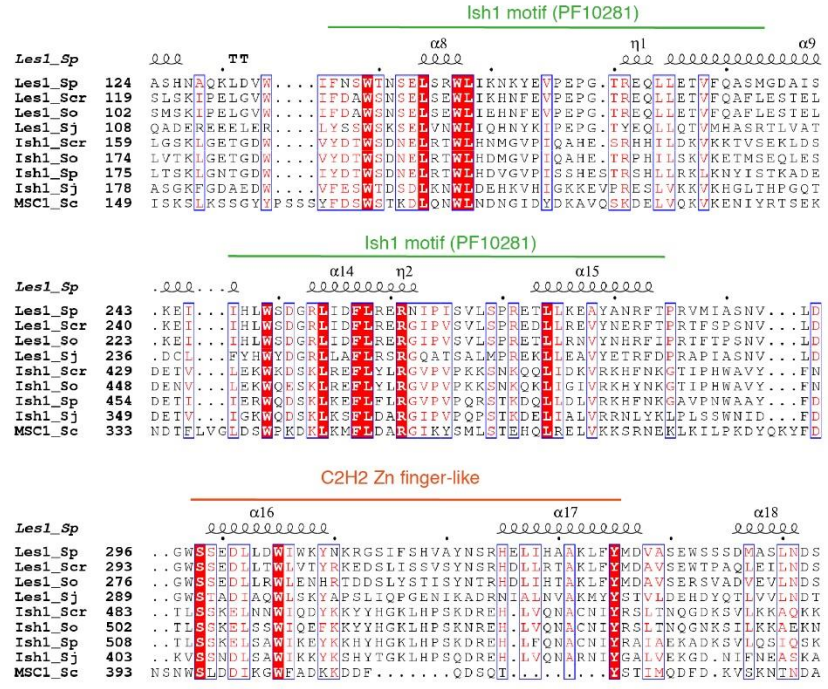

Extended Data Figure 2

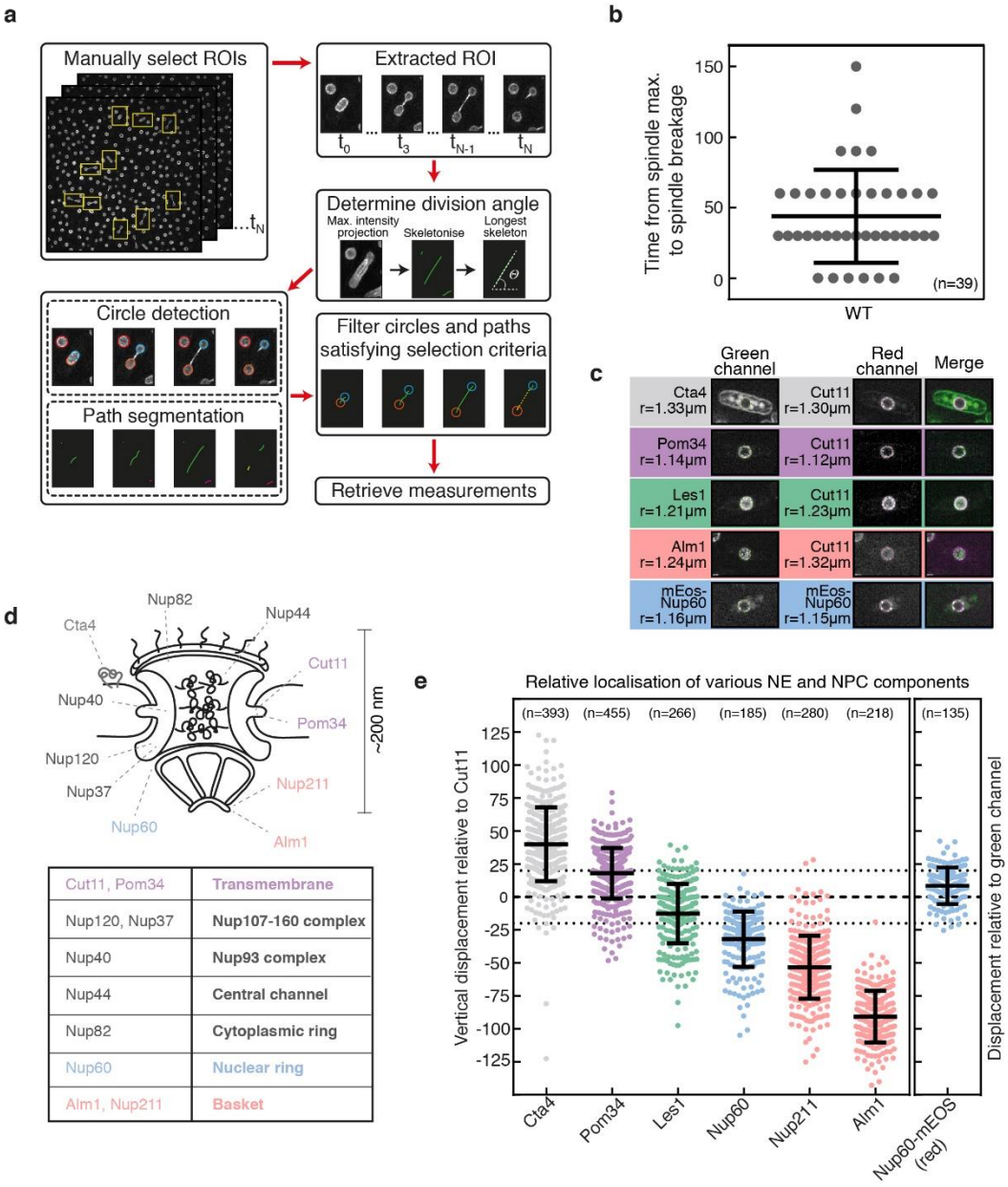

Cut11, Pom34	**Transmembrane**
Nup120, Nup37	**Nup107-160 complex**
Nup40	**Nup93 complex**
Nup44	**Central channel**
Nup82	**Cytoplasmic ring**
Nup60	**Nuclear ring**
Alm1, Nup211	**Basket**

Extended Data Figure 3

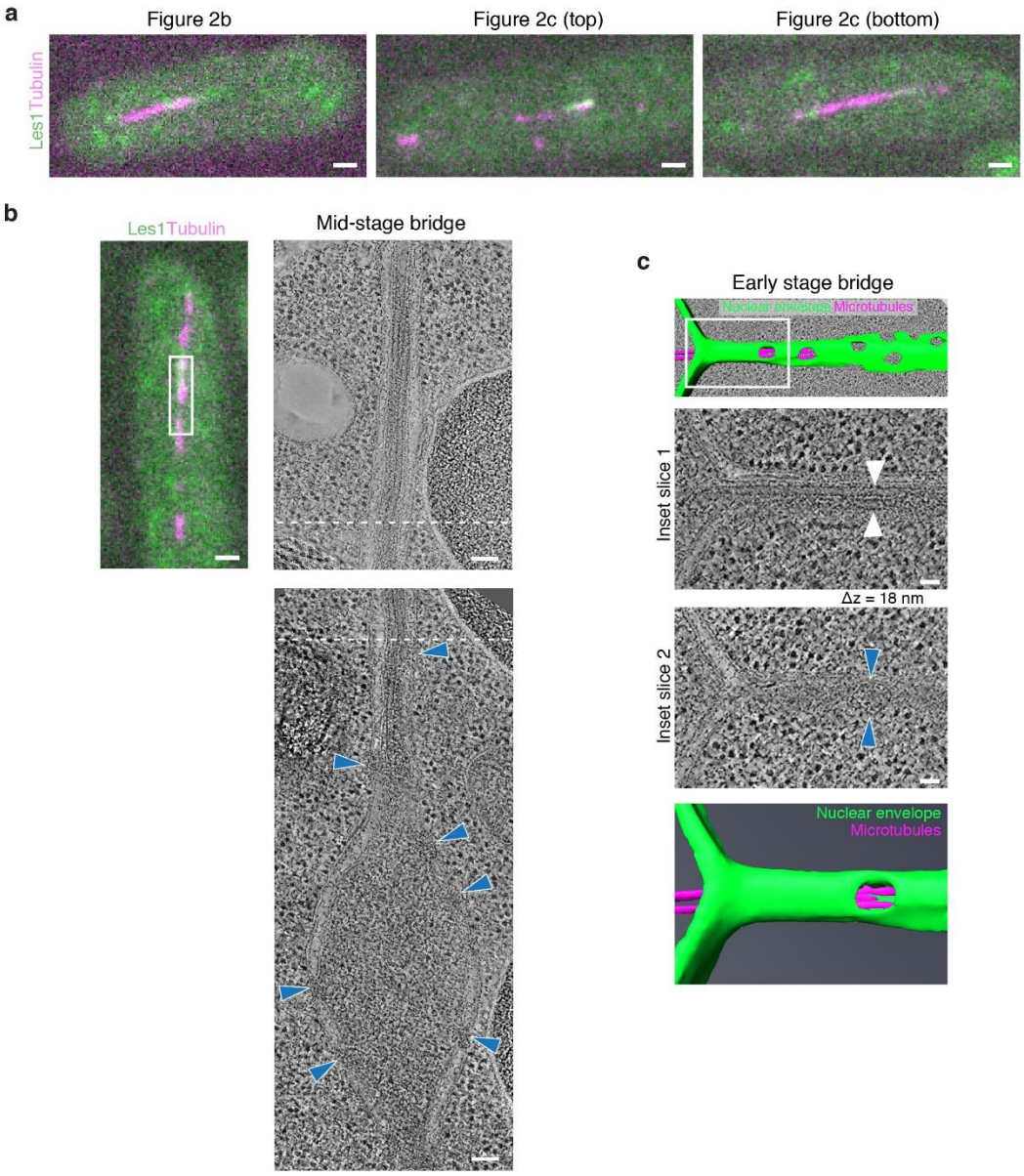

Extended Data Figure 4

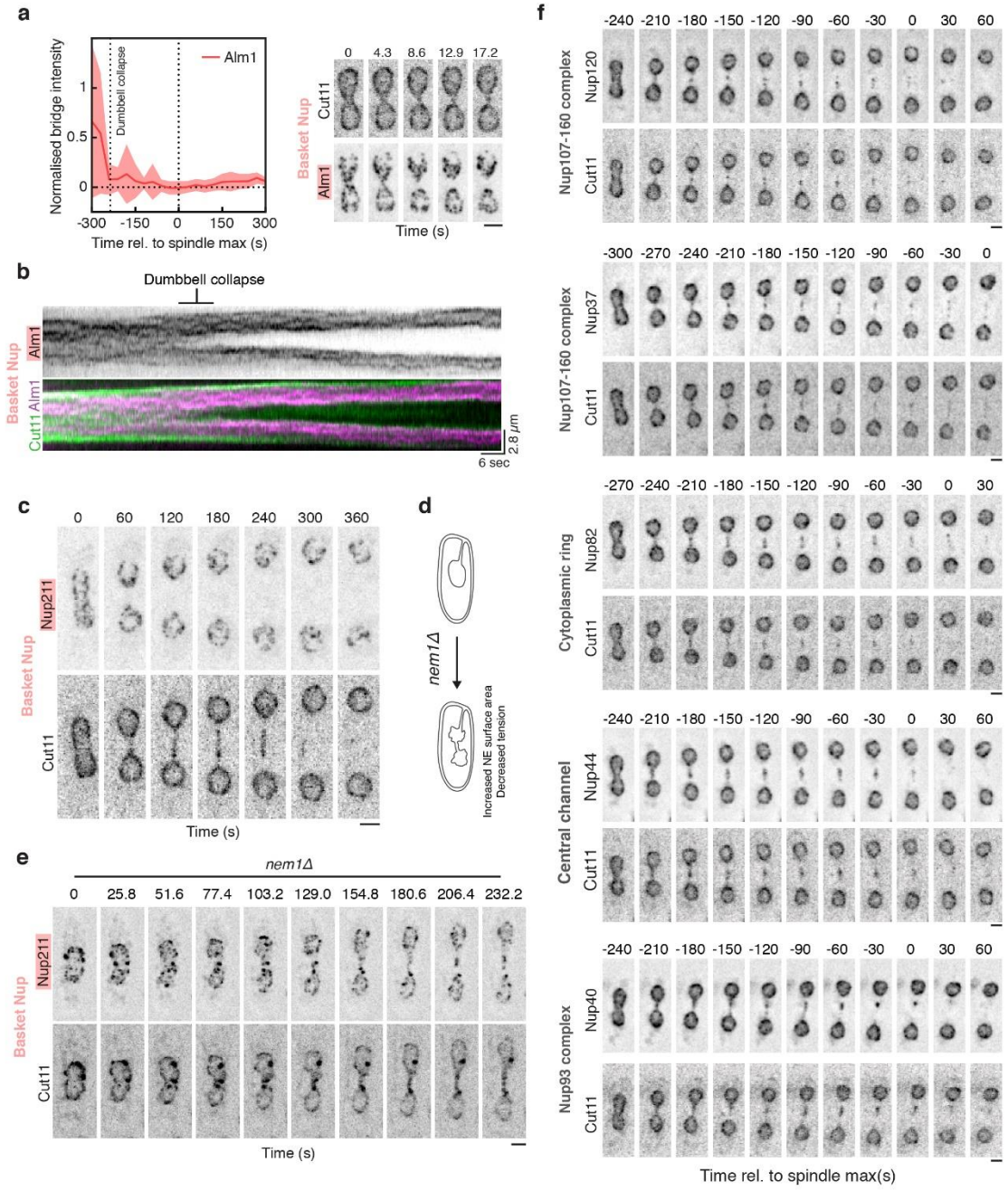

Extended Data Figure 5

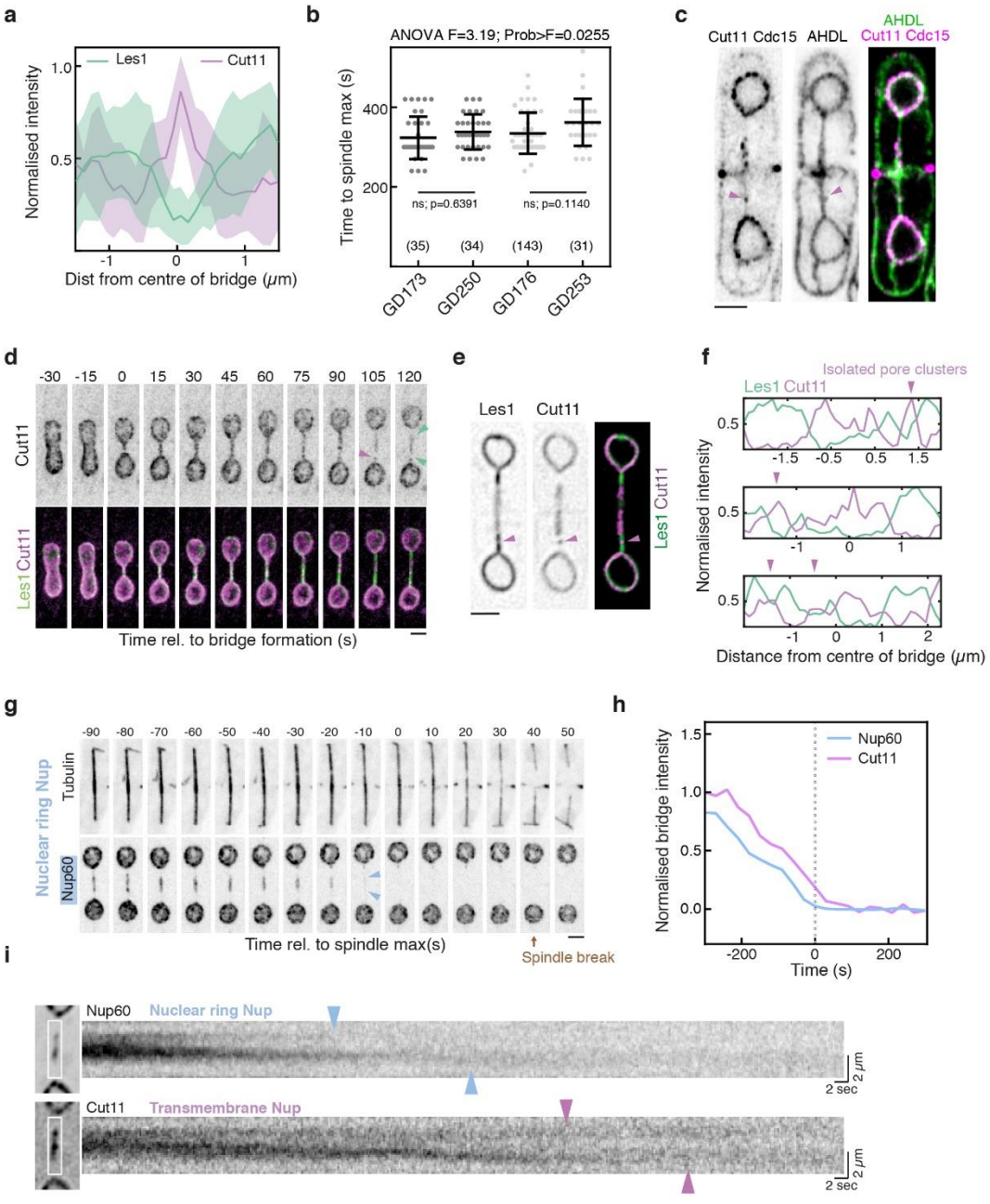

Extended Data Figure 6

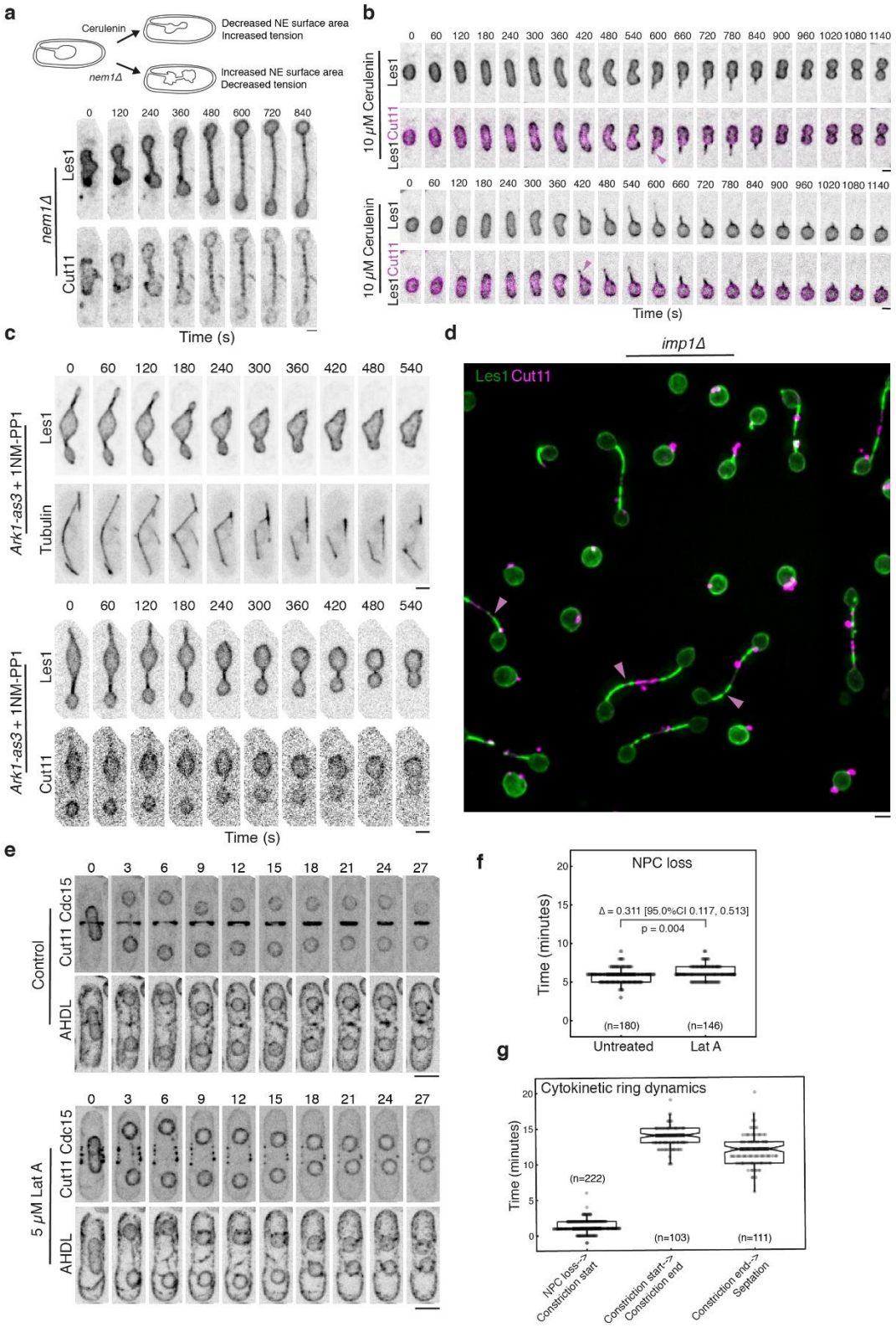

Extended Data Figure 7

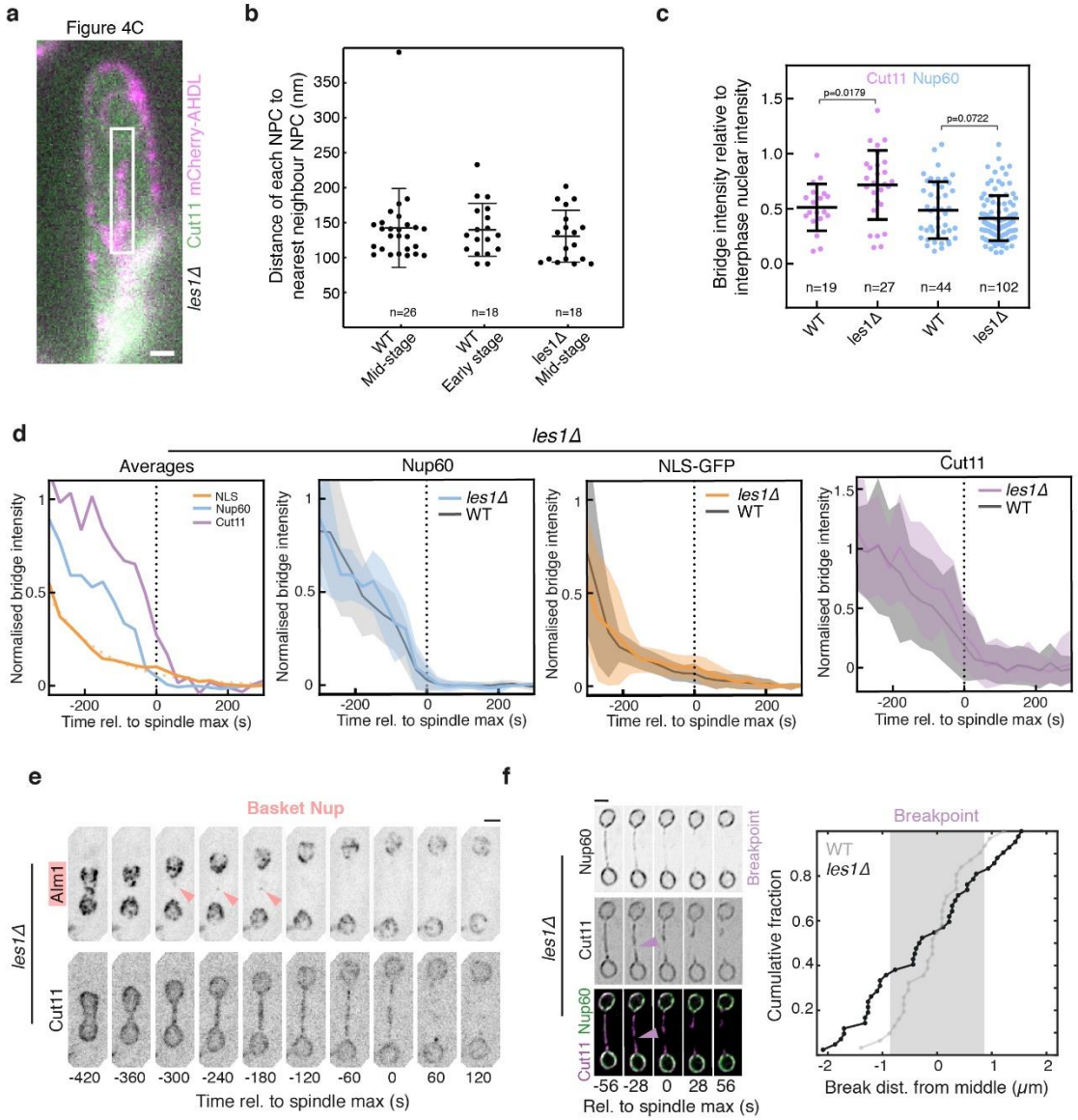

Publisher: NPG; Journal: Nature: Nature; Article Type: Biology article
MS nr: 2019-08-12893D

Extended Data Figure 8

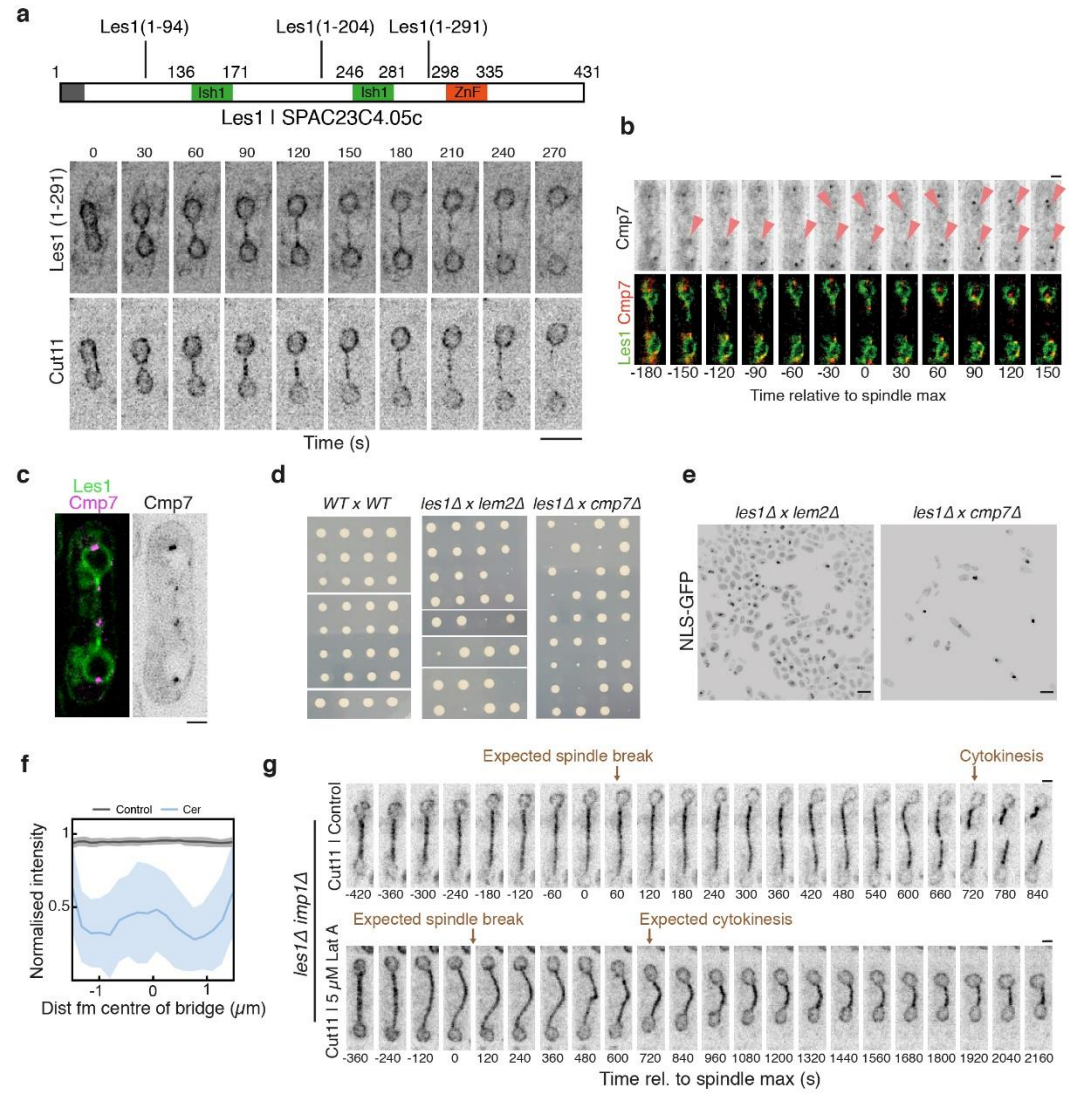

Strain	Genotype	Reference	Strain construction details
SO4913	*cut11-GFP:ura4+ pBiP1-mCherry-AHDL:leu1+ h+*	Snezhana Oliferenko lab	*For original AHDL*[32]
SO6600	*pBiP1-NLS-GFP-NLS:leu1+_ade-_leu1-32_ura4D-18 h-*	Snezhana Oliferenko lab	*Integration at leu1 locus*
MBY5861	*cut11-mCherry:ura4+ h-*	Mohan Balasubramanian lab	
MBY6659	*pAct1 Lifeact-GFP:leu+ atb2-mCherry:Hph leu1-32 ura4-D18 h-*	Mohan Balasubramanian lab	*pCDL1484 integrated into MBY5856*
SI235	*Hph<<ark1-as3 h-*	Silke Hauf lab	*Hph integrated 390 bp upstream of Ark1 start codon; mutations are L166A (gatekeeper), S229A Q28R Q176R (suppressor)*
SI236	*Hph<<ark1-as3 h+*	Silke Hauf lab	*Hph integrated 390 bp upstream of Ark1 start codon; mutations are L166A (gatekeeper), S229A Q28R Q176R (suppressor)*
PN1	*972 h- (wild type)*	Paul Nurse lab	
PN2	*972 h+ (wild type)*	Paul Nurse lab	
GD111	*Hph<<ark1-as3 atb2-mCherry:Hph h?*	This study	*MBY6659 X SI236*
GD121	*cut11-mNeonGreen:Kan Hph<<ark1-as3 atb2-mCherry:Hph h?*	This study	*cut11-mNeonGreen:Kan transformed into GD111*
GD130	*les1-mNeonGreen:Kan Hph<<ark1-as3 atb2-mCherry:Hph h?*	This study	*les1-mNeonGreen:Kan transformed into GD111*
GD138	*les1-mNeonGreen:Kan h+*	This study	*les1-mNeonGreen:Kan transformed into 972 h+*
GD141	*les1-mNeonGreen:Kan atb2-mCherry:Hph h?*	This study	*GD138 X MBY6659*
GD155	*Hph<<ark1-as3 pBiP1-mCherry-AHDL::leu1+ h+*	This study	*SO4913 X SI235*
GD171	*les1::Hph cut11-mCherry:ura4+ h-*	This study	*les1::Kan transformed into MBY5861*
GD172	*les1-mNeonGreen:Kan cut11-mCherry:ura4+ h+*	This study	*GD138 X MBY5861*
GD173	*nup60-mNeonGreen:Kan cut11-mCherry:ura4+ h-*	This study	*nup60-mNeonGreen:Kan transformed into MBY5861*
GD175	*nup60-mNeonGreen:Kan Hph<<ark1-as3 atb2-mCherry:Hph h?*	This study	*nup60-mNeonGreen:Kan transformed into GD111*
GD176	*nup60-mNeonGreen:Kan les1::Hph cut11-mCherry:ura4+ h-*	This study	*nup60-mNeonGreen:Kan transformed into GD171*
GD206	*les1::Hph pBiP1-NLS-GFP-NLS:leu1+_ade-_leu1-32_ura4D-18 h-*	This study	*les1::Hph transformed into SO6600*
GD220	*alm1-mNeonGreen:Kan cut11-mCherry:ura4+ h-*	This study	*alm1-mNeonGreen:Kan transformed into MBY5861*
GD224	*nup211-mNeonGreen:Kan cut11-mCherry:ura4+ h-*	This study	*nup211-mNeonGreen:Kan transformed into MBY5861*
GD225	*pom34-mNeonGreen:Kan cut11-mCherry:ura4+ h-*	This study	*pom34-mNeonGreen:Kan transformed into MBY5861*
GD227	*cdc15-mNeonGreen:Kan cut11-mCherry:ura4+ h-*	This study	*cdc15-mNeonGreen:Kan transformed into MBY5861*
GD229	*nup60-mEOS3.2:Kan h+*	This study	*nup60-mEOS3.2:Kan transformed into 972 h+*
GD250	*nup60-mCherry:Kan h+ pBiP1-NLS-GFP-NLS:leu1+_ade-_leu1-32_ura4D-18 h-*	This study	*nup60-mCherry:Kan transformed into SO6600*
GD253	*les1::Hph nup60-mCherry:Kan h+ pBiP1-NLS-GFP-NLS:leu1+_ade-_leu1-32_ura4D-18 h-*	This study	*les1::Hph transformed into GD250*
GD255	*les1-mNeonGreen:Kan Hph<<ark1-as3 pBiP1-mCherry-AHDL::leu1+ h+*	This study	*les1-mNeonGreen:Kan transformed into GD255*
GD257	*cta4-mNeonGreen:Kan cut11-mCherry:ura4+ h-*	This study	*cta4-mNeonGreen:Kan transformed into MBY5861*
GD259	*nup60-mCherry:Hph les1::NatR cmp7-mNeonGreen:Kan h-*	This study	*nup60-mCherry:Hph transformed into GD273*
GD261	*nup120-mNeonGreen:Kan cut11-mCherry:ura4+ h-*	This study	*nup120-mNeonGreen:Kan transformed into MBY5861*
GD263	*nup82-mNeonGreen:Kan cut11-mCherry:ura4+ h-*	This study	*nup82-mNeonGreen:Kan transformed into MBY5861*
GD264	*nup37-mNeonGreen:Kan cut11-mCherry:ura4+ h-*	This study	*nup37-mNeonGreen:Kan transformed into MBY5861*
GD265	*nup44-mNeonGreen:Kan cut11-mCherry:ura4+ h-*	This study	*nup44-mNeonGreen:Kan transformed into MBY5861*
GD266	*nup40-mNeonGreen:Kan cut11-mCherry:ura4+ h-*	This study	*nup40-mNeonGreen:Kan transformed into MBY5861*
GD270	*nem1::Hph nup211-mNeonGreen:Kan cut11-mCherry:ura4+ h-*	This study	*nem1::Hph transformed into GD224*
GD273	*les1::NatR cmp7-mNeonGreen:Kan h-*	This study	*les1::NatR transformed into KG18766*
KG18766	*cmp7-mNeonGreen:Kan h-*	Kathy Gould lab	*cmp7-mNeonGreen:Kan transformed into 972 h-*
GD275	*nem1::Hph les1-mNG:kanR cut11-mCh:ura4+ h+*	This study	*nem1::Hph transformed into GD172*
GD181	*imp1::Kan les1::Hph cut11-mCherry:ura4+ h-*	This study	*imp1::Kan transformed into GD171*
GD139	*les1:mScarlet:Hph h+*	This study	*les1:mScarlet:Hph transformed into 972 h+*

GD140	*cmp7-mNeonGreen:Kan les1:mScarlet:Hph h+*	This study	*KG18766 crossed with GD139*
GD283	*les1(1-204):mNeonGreen cut11-mCherry:ura4+ h-*	This study	*les1(1-204):mNeonGreen transformed into MBY5861*
GD284	*les1(1-291):mNeonGreen cut11-mCherry:ura4+ h-*	This study	*les1(1-291):mNeonGreen transformed into MBY5861*
GD285	*les1(1-94):mNeonGreen cut11-mCherry:ura4+ h-*	This study	*les1(1-94):mNeonGreen transformed into MBY5861*
GD290	*imp1::Hph alm1-mNeonGreen:Kan cut11-mCherry:ura4+ h-*	This study	*imp1::Hph transformed into GD220*
GD292	*imp1::Hph les1-mNeonGreen:Kan cut11-mCherry:ura4+ h+*	This study	*imp1::Hph transformed into GD172*
GD196	*les1::Hph cut11-GFP:ura4+ pBiP1-mCherry-AHDL:leu1+ h+*	This study	*les1::Hph transformed into SO4913*